Marine and Petroleum Geology 144 (2022) 105834

Contents lists available at ScienceDirect

Marine and Petroleum Geology

journal homepage: www.elsevier.com/locate/marpetgeo

Diatom influence on the production characteristics of hydrate-bearing sediments: Examples from Ulleung Basin, offshore South Korea

Junbong Jang [a], William F. Waite [b], Laura A. Stern [c], Joo Yong Lee [d,*]

[a] Department of ICT Integrated Safe Ocean Smart Cities Engineering, Dong-A University, Busan, South Korea
[b] U.S. Geological Survey, Woods Hole, MA, USA
[c] U.S. Geological Survey, Menlo Park, CA, USA
[d] Climate Change Response Division, Korea Institute of Geoscience and Mineral Resources (KIGAM), Daejeon, South Korea

ARTICLE INFO

Keywords:
The second Ulleung Basin Gas Hydrate drilling expedition (UBGH2)
Gas hydrate
Fine-grained sediments
Diatoms
Pore-fluid chemistry
Compressibility
Permeability

ABSTRACT

The Ulleung Basin Gas Hydrate field expeditions in 2007 (UBGH1) and 2010 (UBGH2) sought to assess the Basin's gas hydrate resource potential. Coring operations in both expeditions recovered evidence of gas hydrate, primarily as fracture-filling (or vein type) morphologies in mainly silt-sized, fine-grained sediment, but also as pore-occupying hydrate in the coarser-grained layers of interbedded sand and fine-grained systems. A commonality across many of these occurrences is the presence of diatoms in the fine-grained sediment. Here we tested fine-grained sediment (median grain size <12.5 μm) associated with hydrate occurrences at four UBGH2 sites (UBGH2-2-2, UBGH2-3, UBGH2-6 and UBGH2-11) to investigate potential impacts of diatoms on efforts to extract methane from hydrate, or to tap hydrocarbon reservoirs beneath hydrate-bearing sediment. Two key considerations are: the extent to which diatoms control sediment mechanical properties, and the extent to which pore-water freshening, which occurs as gas hydrate breaks down during resource extraction, alters the diatom control on sediment mechanical properties. We conducted experiments to measure sediment index properties, sedimentation behavior and compressibility to address these considerations. We relied on scanning electron microscope (SEM) imagery and X-ray powder diffraction (XRD) to characterize the sediment mineralogy. Our high-level findings are that at the ~20–45% (by volume) diatom concentrations observed at these UBGH2 sites, sediment compressibility increases with diatom content, but diatoms only appear to increase porosity and permeability at the highest diatom concentration (~45%). Our measurements suggest in situ compression indices of 0.35–0.55 and permeabilities on the order of 0.01milliDarcies (1×10^{-17} m^2) can be anticipated at these sites. Importantly, these properties are not expected to vary significantly upon pore water freshening that accompanies gas hydrate dissociation during production.

1. Introduction

Methane gas hydrate is a naturally-occurring crystalline solid in which methane molecules are encaged in a lattice of water molecules (Sloan and Koh, 2007). The methane hydrate stability and formation requirements of moderate temperature, elevated pressure and sufficient methane and water supply (Kvenvolden, 1993) are met in continental margin and permafrost-associated sediment, yielding a global distribution of methane hydrate (Kvenvolden et al., 1993; Waite et al., 2020; Wallmann et al., 2012). In 2005, South Korea began a "10-year Korean National Gas Hydrate Program" as part of a national effort to reduce dependence on foreign energy resources, carrying out the Ulleung Basin Gas Hydrate expeditions (UBGH1 in 2007, UBGH2 in 2010) to assess the domestic resource potential of methane hydrate (Ryu et al., 2013).

South Korea signed the Paris Agreement, seeking to limit the global temperature change to less than 1.5 °C above levels prior to the Industrial Revolution (Falkner, 2016; United Nations, 2016). Methane is seen as a viable bridge fuel, a transitional energy with lower net carbon emission than oil and coal (Levi, 2013; Tanaka et al., 2019; Kastner et al., 2022), that could be used while existing challenges to a direct conversion from fossil fuels to renewable energy (summarized by Halkos and Gkampoura (2020)) are addressed. For the extraction of methane from gas hydrate to be commercially viable however, a number of technical challenges must be overcome (Hancock et al., 2019), including

* Corresponding author.
E-mail address: jyl@kigam.re.kr (J.Y. Lee).

https://doi.org/10.1016/j.marpetgeo.2022.105834
Received 25 March 2022; Received in revised form 20 June 2022; Accepted 12 July 2022
Available online 20 July 2022

the potential for production flow rate limitations due to reservoir compression (e.g. Boswell et al., 2019; Flemings et al., 2020; Myshakin et al., 2019), clogging due to the migration of sediment particles (e.g., Cao et al., 2019; Jang et al., 2020a; Jung et al., 2012; Uchida et al., 2019; Valdes and Santamarina, 2007), and lack of reservoir pressure isolation from bounding sedimentary units (e.g., Ajayi et al., 2018; Jang et al., 2020b; Konno et al., 2019; Moridis et al., 2019a). Conventional hydrocarbon production can also be hampered if the production well design and operations do not account for gas hydrate in the overlying sediment (Hadley et al., 2008).

Potentially significant contributions to these production challenges depend on the type, concentration, and distribution of fine-grained particles, or "fines," at the production site. Fines are particles smaller than 75 μm-diameter and include silt and clay in the unified soil classification system (USCS; ASTM, 2011a). Whereas course-grained particle interactions are dominated by gravitational forces, fines are small enough to be influenced by electrical forces due to their unbalanced surface charges (Lambe and Whitman, 1969). The magnitude and distribution of these surface charges depend on the particle mineralogy and size, so the particle characteristics as well as the pore fluid chemistry between the particles all affect the particle arrangements (sediment fabric) and consequently affect sediment properties such as compressibility, permeability, and particle mobility (reviewed in Cao et al. (2019); Jang et al. (2018)).

The dependence of these properties on fines is particularly significant when extracting methane from gas hydrate via reservoir depressurization, which is seen as the most promising production technique (Boswell et al., 2014; Yamamoto et al., 2019). The depressurization method reduces in situ pore pressure, destabilizing methane hydrate so it releases methane gas and pure water. Mechanically, the depressurization method increases vertical effective stress, particularly in deep-water systems such as the Ulleung Basin because the pore pressure must be reduced by several MPa or more to destabilize gas hydrate in these environments (Boswell et al., 2019; Moridis et al., 2019b). The effective stress increase compresses the affected sediments, which the well structure must be designed to accommodate (Hancock et al., 2019), and also reduces reservoir permeability due to the porosity loss (Yoneda et al., 2019b). Myshakin et al. (2019) showed the permeability reduction can be significant, with permeability dropping by two orders of magnitude during depressurization for a modeled production test offshore India.

Pore-water chemistry also changes as methane hydrate breakdown releases fresh water, reducing the in-situ salinity by 55–65% for methane hydrate saturations of 60–70% (Jang et al., 2020a). Depending on the electrical sensitivity of the fines (Jang and Santamarina, 2016a; Jang et al., 2018), interactions between fines can be sensitive to the pore water salinity, leading to a range of potential reservoir property changes as the pore water freshens. Pore-water freshening can alter the fines compressibility (Bolt, 1956; Olson and Mesri, 1970), the tendency for fines to resuspend and become entrained with fluids and gas flowing toward the production well (Mohan et al., 1993; Jang et al., 2020a), and the capacity for fines to cluster and clog pore throats to reduce reservoir permeability (Lambe and Whitman, 1969; Cao et al., 2019).

In this work, we focus on the impact of diatoms, a type of photosynthetic microalgae found in the photic zone of the water column, on sediment properties. When diatoms die, they leave behind a porous, silica-based skeleton that can settle to the seafloor and get incorporated into the sediment. The global distribution of diatom skeletons in sediment depends on geologic, oceanic and climate conditions that can affect productivity of diatoms (Cortese et al., 2004; Cawthern et al., 2014) and whether or not their skeletons dissolve before they reach the seafloor (Kamatani and Riley, 1979; Treguer et al., 1995). Diatom skeletons (or "frustules," but simply referred to as "diatoms" in this work), exhibit a wide variety of morphologies (Fig. 1. See also Fig. 6 in Jang et al., 2020a), but typically have lower density than the surrounding sediment grains due to the pores, holes and other "internal porosity" (Fig. 1) that the diatom skeletons have for their strength and protection (Zglobicka et al., 2017).

The structure and arrangement of diatoms, particularly in fine-grained sediment, have significant impact not only on where and how much gas hydrate can accumulate in the sediment, but also on how the host sediment will respond when the hydrate breaks down naturally or as a result of human energy recovery efforts. As an example, the presence of internal pores and pore space formed from enmeshed diatoms (Fig. 1) provides gas hydrate nucleation surfaces (Bahk et al., 2013a.; Dai et al., 2014) and pore spaces that are larger than what is typically available in diatom-free fine-grained sediment (Lei and Santamarina, 2018; Kraemer et al., 2000). As an example, Kraemer et al. (2000) observed that hydrate was present in diatom-rich layers and absent from intervening, diatom-poor layers along the Blake Ridge, offshore eastern USA. Mechanistically, diatoms enhance hydrate formation because the larger pore spaces they create allow for hydrate to grow at lower levels of pore-water methane concentration (Kraemer et al., 2000) than in the surrounding fine-grained sediment. In the aspect of mechanical behavior of sediments relevant to energy extraction activities, the composition and structure of diatoms strongly increases overall sediment compressibility (Kwon et al., 2011; Lee et al., 2011), and can also enhance pore-throat clogging that reduces the efficiency of extracting methane from gas hydrate (Cao et al., 2019).

To gain insight into the potential impact of diatoms on a range of potential hydrate-associated gas hydrate dissociation and gas production processes in the Ulleung Basin, we performed a suite of index

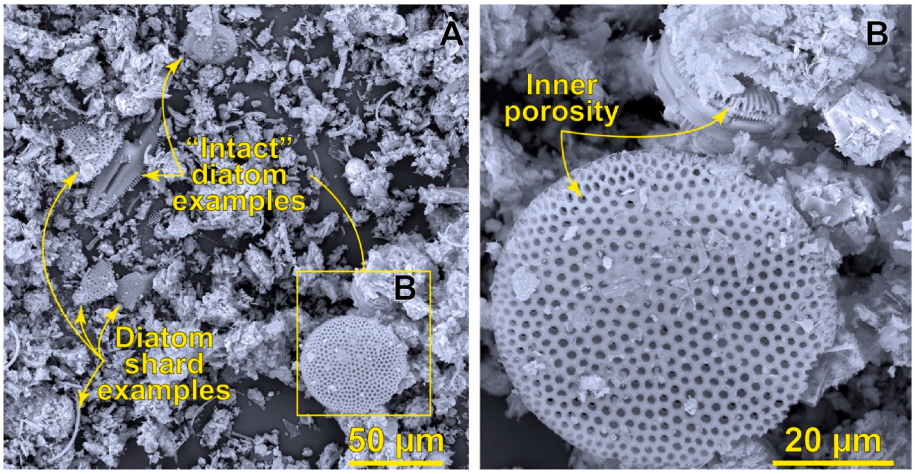

Fig. 1. Examples of diatoms and diatom shards from UBGH2-6. A) Diatom shards and ribbons, a few of which are highlighted, have irregular shapes that can easily become entangled, preserving a more porous sediment fabric than would likely occur in the absence of diatoms. B) Diatoms, which can be tens of micrometers across, often have perforated or tubular structures that preserve void volume within the diatoms themselves. As the diatom concentration in the sediment increases, this "inner porosity" structure contributes more significantly to sediment void space, to surface area, and can alter the sediment's mechanical properties.

property, imagery, sedimentation, and compressibility studies on sediment from four UBGH2 sites (Table 1). The four sites chosen for this study cover a range of hydrate morphologies and energy resource potential: two sites (UBGH2-2-2 and UBGH2-6) have gas hydrate concentrated in thin, coarse-grained layers interbedded with fine-grained sediment, and UBGH2-6 has been considered a potential production test site. Two sites (Sites UBGH2-3 and UBGH2-11) are associated with gas hydrate-filled veins and fractures in fine-grained sediment adjacent to a gas hydrate chimney, and one site (Site UBGH2-3) has hydrate-filled veins and fractures in fine-grained sediment associated with an underlying conventional petroleum field (Ryu et al., 2013).

2. Geologic setting

The tectonic history of the Ulleung Basin, a back-arc basin in the East Sea (Fig. 2), is described in detail by Chough and Barg (1987) and has been reviewed in reference to the UBGH1 and UBGH2 expeditions by Ryu et al. (2009) and Bahk et al. (2013a). For this study, it is important to note the effects of tectonic compression on the Ulleung Basin beginning in the late Miocene (Chough and Barg, 1987). Compression caused uplift in the southern part of the basin, and combined with rapid sedimentation, led to a series of mass transport events that reworked and moved sediment toward the north (Lee et al., 2001).

Sediment transport in the central and northern portions of the Ulleung Basin since the late Miocene generally resulted in turbidite flows separated by intervals of hemipelagic sedimentation (Lee et al., 2001), creating a layered series of coarse- and fine-grained sediment. Basin compression has continued to the present time (Ingle, 1992), inducing sediment deformation and faulting, driving upward fluid flow while creating permeable pathways that are thought to promote fluid migration into the observed zones of methane hydrate occurrence in UBGH1 and UBGH2 (Ryu et al., 2009; Yoo et al., 2013). The sedimentary environments for the four UBGH2 sites in this study are summarized in Fig. 3, Table 2, and as follows:

2.1. UBGH2-2-2

UBGH2-2-2, like UBGH2-11 (Section 2.4), is adjacent to site UBGH1-9, a chimney structure with no surface expression that was cored during the first UBGH expedition (Kim et al., 2011; Riedel et al., 2012). UBGH2-2-2 is outside the chimney region, in a zone of flat-lying seismic reflections (see Fig. 3 in Kim et al., 2013c) potentially indicating hydrate-bearing, coarse-grained units. Coring results revealed the site was primarily fine-grained pelagic sediment, though a few thin (1–14 cm thick, averaging 3 cm thick), coarser-grained layers of sand and ash were also present (Ryu et al., 2013). Gas hydrate was associated with some of those coarse-grained layers (Bahk et al., 2013a; Lee et al., 2013b; Ryu et al., 2013), and was also disseminated in diatom-rich silts and found as fracture-fill in fine-grained sediment (Bahk et al., 2013a). The site is used here, along with UBGH2-6 (Section 2.3), to examine how diatom-rich sediment could impact efforts to extract methane from hydrates in thin, coarse-grained units within primarily fine-grained systems.

Table 1
Site locations and water depths for the Ulleung Basin Gas Hydrate Expedition 2 (UBGH2) sites sampled in this study.

Site Name	Latitude	Longitude	Water Depth (m)
UBGH2-2-2B	36° 42.7067′ N	130° 53.7100′ E	2092.2
UBGH2-3C	36° 41.2683′ N	130° 20.6417′ E	897.8
UBGH2-6B	37° 00.9600′ N	130° 16.0000′ E	2154.2
UBGH2-6C	37° 00.9583′ N	130° 15.9833′ E	2152.8
UBGH2-11B	36° 39.7833′ N	130° 54.4150′ E	2082.6

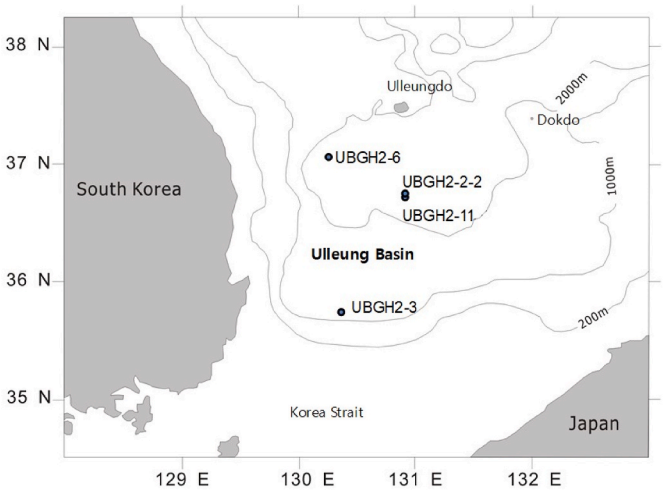

Fig. 2. Four locations of the fine-grained samples collected during UBGH2 and used in this study. Contours indicate water depth in meters.

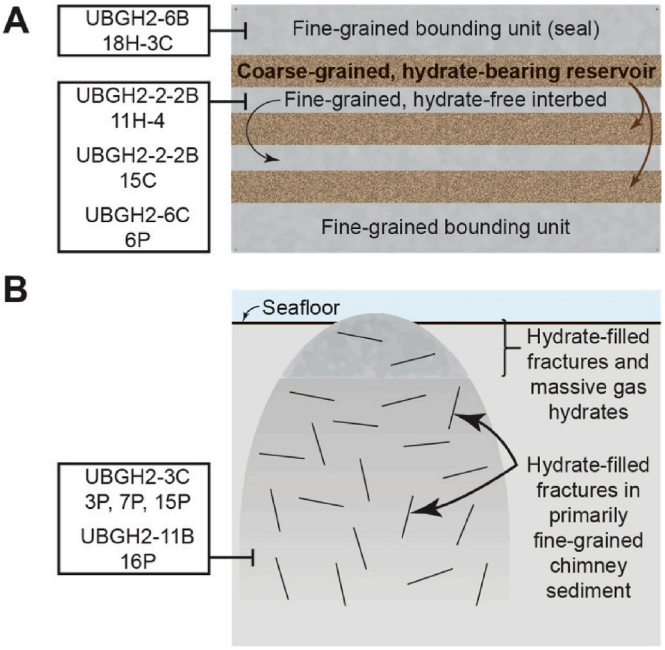

Fig. 3. Schematic sample locations relative to gas hydrate accumulations. (A) Layered reservoir with pore-occupying gas hydrate in coarse-grained sediment separated by fine-grained hydrate-free interbed sediment. Reservoir system is capped by a fine-grained "seal" layer (e.g., sites UBGH2-2-2B and UBGH2-6). (B) Chimney environment, with grain-displacing gas hydrate potentially forming massive gas hydrate near the seafloor and hydrate-filled fractures in the chimney's predominantly fine-grained sediment (e.g., UBGH2-3 and UBGH2-11).

2.2. UBGH2-3

The southern-most site in this study is a seismically-imaged chimney structure that reaches the surface as a mound (see Fig. 3 in Kim et al., 2013a). Logging results indicating the chimney hosts gas hydrate in many small vertical fractures (Lee and Collett, 2013), were confirmed in pressure cored samples containing numerous hydrate-filled fractures in fine-grained sediment (Lee et al., 2013b). Around 10 and 13 meters below seafloor, mbsf, hydrate appears to displace enough sediment to appear as "massive" gas hydrate occurrences (Lee and Collett, 2013) that can be on the order of tens of cm thick when cored (e.g., Fig. 6 in Ryu

Table 2
Sample identification, sediment type and technical notes. Base of Gas Hydrate Stability Zone (BGHSZ) is taken from Ryu et al. (2013).

Sediment Type	Sample Identification			Depth [mbsf]	Depth of BGHSZ [mbsf]	Remarks
	Site	Core	Depth in core [cm]			
Fine-grained seal	UBGH2-2-2B	11H-4	81–95	117	180.5	combined as one sample
	UBGH2-2-2B	11H-4	101–117			
Fine-grained interbed	UBGH2-2-2B	15C	45–57	141.5	180.5	also used for micromodel flow-clogging tests (Jang et al., 2020a)
	UBGH2-6B	18H-3C	0–20	131	167	
	UBGH2-6C	6P	40–85	152.4	167	
Fine-grained chimney sediment	UBGH2-3C	3P	0–25	44	131.6	
	UBGH2-3C	7P	20–62	61.2	131.6	
	UBGH2-3C	15P	10–48	92.1	131.6	
	UBGH2-11B	16P	30–50	76.3	159	

et al., 2013). UBGH2-3 is associated with the neighboring Donghae-1 commercial gas field and was initially thought to be supplied by thermogenic gas, but no thermogenic gases were ultimately identified at the site (Ryu et al., 2013). Nonetheless, the site is used here to examine how hydrates in diatom-rich sediment can impact the production of underlying conventional hydrocarbons.

2.3. UBGH2-6

UBGH2-6 is located in the northern part of the Ulleung Basin, where Lee et al. (2001) mapped flat-lying sequences of coarse-grained turbidite layers separated by fine-grained hemipelagic sediment. Strong seismic reflections just above the base of hydrate stability (see Fig. 1 in Lee and Collett, 2013) indicated gas hydrate could be present in the coarse-grained layers. Coring revealed coarse-grained layers 1–148 cm thick, averaging 9 cm thick (Ryu et al., 2013), with two hydrate-bearing intervals exceeding 30 cm each (Lee et al., 2013b). The hydrate-bearing layers were interbedded with fine-grained, hydrate-free hemipelagic layers that varied from the centimeter- to meter-scale in thickness (Bahk et al., 2013b; Ryu et al., 2013). UBGH2-6 has been considered for a potential production test to extract methane from hydrate (Ryu et al., 2013), and is used here to illustrate how diatoms can influence production from an interbedded coarse- and fine-grained reservoir.

2.4. UBGH2-11

UBGH2-11 targets a chimney structure adjacent to UBGH1-9 that seismic images suggest reaches the seafloor (see Fig. 4 in Kim et al., 2013a). The chimney sediment is primarily fine-grained, though does host thin, discrete coarse-grained bodies (Lee et al., 2013b). Hydrate is primarily observed as fractures displacing fine-grained sediment, with thin, isolated, hydrate-free sand bodies observed adjacent to the hydrate-filled fractures (Lee et al., 2013b). As observed at UBGH2-3, grain-displacing hydrate occurrences have grown in the upper portion of the chimney to represent massive, nearly sediment-free bodies of gas hydrate (Kim et al., 2013a). UBGH2-11 is used here to illustrate the impact of diatoms on the potential for extracting methane from hydrate filled fractures as well as from massive gas hydrate occurrences in fine-grained sediment.

3. Materials

Table 2 summarizes the sample identification and recovery depths for the sediment samples tested here. To facilitate the discussion of diatom effects on reservoir productivity, we classify our study material according to a series of idealized elements of hydrate-bearing reservoir systems (sediment classifications are shown schematically in Fig. 3).

An important consideration when attributing an idealized element classification to the sediments in this study (first column in Table 2) is the length scale over which that sediment lithology occurs. With the exception of the massive gas hydrates (e.g., UBGH2-3 and UBGH2-11), and the thicker sands observed at UBGH2-6 (some exceeding 30 cm thickness), many of the sediment lithologies cored during UBGH2 were coherent only over the scale of several centimeters or less. Predominantly fine-grained sediment units were interspersed with hydrate-bearing fractures (e.g., UBGH2-3), or isolated, thin sand bodies (e.g., upper UBGH2-2-2 sample and UBGH2-11), or were sandwiched between coarse-grained turbidite layers (e.g., lower UBGH2-2-2 sample and UBGH2-6). Isolating these lithologies for study requires undisturbed sediment core sections.

In the absence of gas hydrate, conventional coring technology retains in situ sediment layering, though with drilling disturbances. When hydrate-bearing conventional cores are brought to the drilling ship, methane hydrate present in the core can further disturb the sediment as the hydrate dissociates due to lack of in situ pressure. As noted for UBGH2 by Bahk et al. (2013b), hydrate dissociation during core recovery obscured the in situ sediment layering. Pressure coring, which preserves sediments at or near their in situ pore pressure, can help preserve in situ gas hydrate and the adjacent sedimentary layers during coring for geotechnical property measurements (e.g., Schultheiss et al. (2009); Santamarina et al. (2012); the technological history of pressure coring is reviewed in Dai et al. (2017); Thomas et al. (2020)). All specimens tested here were collected in pressure cores.

4. Methods

Our focus here is on compressibility, permeability and how those properties evolve and impact production activities. As shown by measured (Yoneda et al., 2019b) and modeled (Myshakin et al., 2019) results, highly-compressible sediment will experience porosity and permeability reduction that can limit overall production rates when that highly-compressible sediment is exposed to the elevated effective stresses imposed while methane is produced from gas hydrate-bearing sediments (Boswell et al., 2019). To understand what controls the compressibility of fine-grained sediments associated with gas hydrate in the Ulleung Basin, we combine one-dimensional (1D) consolidation tests with the suite of physical property measurements summarized in Table 3. The measurement strategy is summarized here.

We use particle size, specific gravity and specific surface area data to indicate the extent to which the sediment behavior can be influenced by the electrical charge imbalances on individual sediment grains. The general rule is that the most easily-influenced particles are small (fine-grained), low-density, and have high surface area for hosting electrical charges. Larger (coarse-grained), dense, rounded (low surface area) particles such as sands are more influenced by gravitation than electrical forces.

Table 3
Experimental methods used in this study to examine controls on the compressibility of fine-grained UBGH2 sediment associated with gas hydrate in the Ulleung Basin.

Physical property	Experimental approach
Particle size	Laser scattering particle analyzer (Microtrac S3500)
Specific gravity	Gas pycnometer (Pentapycnometer 5200e)
Specific surface area	Methylene blue method (Santamarina et al., 2002)
Particle morphology and elemental constituents	Scanning electron microscope with energy dispersive spectroscope (SEM-EDS, Tescan VEGA-3), optical microscope (Leica DMS 1000)
Mineralogy	X-ray diffraction (XRD, Rigaku Miniflex 600 benchtop X-ray diffraction unit, a Philips X'pert MPD diffractometer)
Fabric changes due to pore fluids	Grain settling based sedimentation test (Jang et al., 2020a)
Liquid limit (LL)	BS 1377, fall cone test (British Standard Institute, 1990)
Plastic limit (PL)	ASTM D4318, thread-rolling test (ASTM, 2010)
Electrical sensitivity to pore fluids	Liquid limit tests with three pore fluids (Jang and Santamarina, 2016a,)
Compressibility	ASTM D2435, 1D consolidation test (ASTM, 2011b)
Permeability	1D consolidation theory (Terzaghi et al., 1996)

Grain-size analysis was conducted onshore using a laser-scattering particle analyzer (Microtrac S3500). The specimens were dried in a freeze drier for 24 h. Dried specimens were treated in 10% H_2O_2 solutions at 80 °C to remove organic material. After removing the organics, specimens were treated in 1 M HCl for 24 h to remove carbonates. Specimens were then cleansed in deionized water until the pH was neutral. To reduce particle clumping, specimens were combined with a 0.1% sodium hexametaphosphate, $(NaPO_3)_6$, solution in a vortex mixer.

Optical and scanning electron microscopy (SEM) imagery indicate particle morphology including individual grain shapes as well as the tendency of particles to clump due to electrical attraction (Jang et al., 2019b). SEM images with energy-dispersive-spectroscopy (EDS) can also reveal the presence of diatoms and identify chemical elements in the samples to support image-based interpretations of sediment content (e.g., Jang et al., 2019a, 2020a).

Mineral compositions were analyzed by X-ray powder diffraction (XRD) and a computer software (SIROQUANT) based on the Rietveld quantification method. For the XRD analysis, a Philips X'pert MPD diffractometer was used with a CuKα radiation source and run at 40 kV and 20 mA. XRD mineralogy data highlight the dominant sediment components. With component information in hand, published compressibility data for pure, endmember fines (e.g., Jang et al., 2018) can be used to anticipate specimen behavior. However, certain sediment components, such as montmorillonite, can be difficult to identify in standard XRD data, or can be difficult to discriminate from similar sediment components (e.g., differentiating mica and illite). XRD interpretations can be qualitatively augmented with the grain-settling-based sedimentation tests, in which sediment is allowed to settle in fluid columns (Fig. 4a).

When free falling in liquid, sediment grains in the grain-settling-based sedimentation tests can segregate based on grain size and electrical sensitivity, forming fabrics due to inter-particle forces such as gravitational and electrical forces (Jang et al., 2018, 2020a). We analyze these grain-settling-based sedimentation tests in conjunction with grain size, mineralogy, and pore-fluid chemistry data. Following the techniques described in Jang et al. (2018, 2020a) for sedimentation tests, a volume of dry sediment was loosely packed into a mold having a 25.4 mm diameter and height as shown in Fig. 4a. That sediment was then allowed to settle in a fluid-filled sedimentation cylinder (Fig. 4a). In this study, we used a range of fluid salinities (deionized water, 0.6 m and 2 m brine, where m is molal, or moles of salt per kilogram of deionized water) to investigate the sediment response to pore-water freshening. We also used the $(NaPO_3)_6$ dispersant to investigate the sediment's capacity to cluster, clump and settle in the absence of interparticle electrical attractions. How sedimentation progresses in different pore fluids determines the sediment fabric, and hence the sediment compressibility (Jang et al., 2018).

As expected for marine sediment and as observed in our XRD results, the in situ pore water was a brine, and salt from that brine precipitated onto the sediment grains when the sediment was dried in the laboratory. Consequently, for the initial sedimentation test, even though the cylinder was filled with deionized water (DW), precipitated salts dissolving off the sediment grains into the cylinder water created a weak brine, which was less saline than the nominal 0.6 m salinity of seawater, and we denote these samples as "deionized water with salt (DWS)." To prepare for the second sedimentation test, the DWS sample's supernatant was removed and replaced with additional DW to create the "deionized water-freshened (DWF)" sample that represents the lowest salinity test in our study. Finally, the supernatant was replaced with 2 m-brine (116.88 g NaCl per kg deionized water) to observe the sedimentation in a high salinity fluid. The cylinder was shaken for 60 s prior to each sedimentation test, then left undisturbed while the depositional and accumulated sediment heights (Fig. 4a) were measured over time.

The extent to which electrical interactions between pore fluids and particles control sediment fabric and compressibility can be quantified via the liquid plastic limit test (empirical correlations are given in Table 4 and discussed in Section 5). As water is added to a soil, the soil transitions from a solid to a semisolid, plastic, and eventually liquid state; the plastic limit, *PL*, is the water content at which the sediment transitions from semisolid to plastic behavior, and the liquid limit, *LL*, similarly indicates the water content separating plastic and liquid behaviors. As Lambe and Whitman (1969) note, a clayey, fine-grained soil that is better able to attract water to the sediment grain surface should have larger plastic and liquid limits, meaning these limits will depend on soil constituents as well as grain size. A related parameter, the plasticity index, $PI = LL\text{-}PL$, gives the range of water contents over which the sediment can be molded into arbitrary shapes.

The liquid limit also provides a quantitative link between the sedimentation test implications for the sediment void ratio (open versus dense fabric) and the ideal initial void ratio for the 1D consolidation test. When the soil is saturated, initial void ratio, e_0, water content, w_c and the specific sediment density, G_s, are related by:

$$e_0 = \frac{Volume_{voids}}{Volume_{solids}} = \frac{mass_{water}}{mass_{solids}} \cdot \frac{density_{solids}}{density_{water}} = w_c \cdot G_s = 1.2 \cdot \frac{LL}{100} \cdot G_s, \quad [1]$$

where we are following the procedure of Jang et al. (2018) in choosing the particular water content $w_c = 1.2 \cdot LL$ as our initial water content when preparing the remolded specimen for a 1D consolidation test. Equation (1) requires unitless parameters, so *LL*/100 is used because *LL* is generally reported in % rather than unitless form. Specimens with higher initial void ratios are generally more compressible (Table 4), though as we see in this study, other factors can contribute to the compressibility. Specimens were reused when the specimen volumes were too small to conduct separate liquid limit tests for the range of fluids used in this study.

Sediment compressibility data can help guide predictions of the reservoir permeability evolution during production (e.g., Boswell et al., 2019; Myshakin et al., 2019), so 1-D incremental loading consolidation tests were run to constrain the sediment compressibility, permeability, and how these parameters change as pore-water freshens during production (Fig. 4b). In this study, pore-water salinity was controlled in two ways for the consolidation tests: using either DW, 0.6 m- or 2 m-brine, the specimen was initially saturated to 120% of the liquid limit water content ($w_c = 1.2 \cdot LL$); then we used either DW, 0.6 m or 2 m brine as the consolidation reservoir fluid (Fig. 4b) to maintain specimen saturation during the consolidation test. To test the response of compressibility to pore water chemistry changes, we replaced the reservoir fluid after the

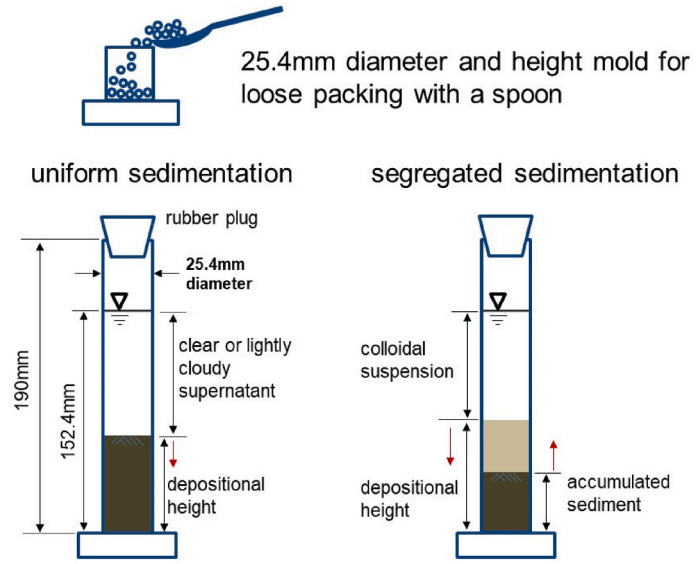

(a) sedimentation test

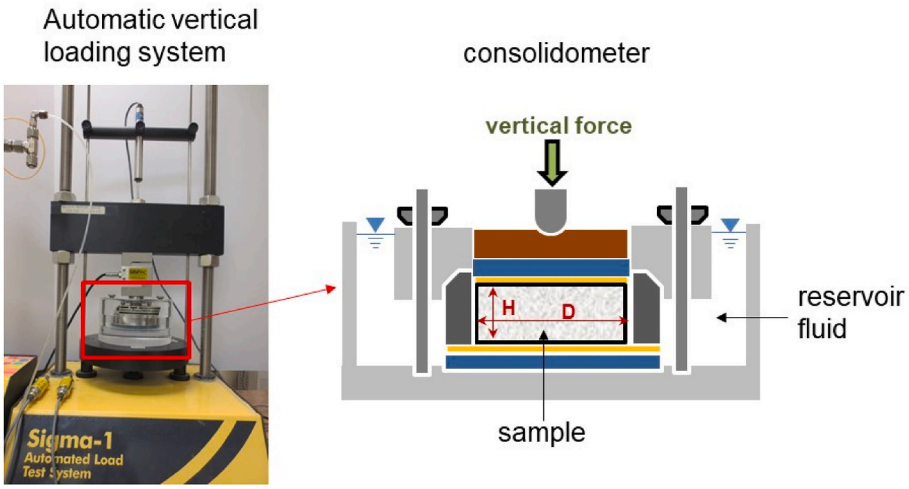

(b) consolidation test

Fig. 4. Experimental configurations: (a) sedimentation test: a mold for obtaining a loose packing of a sample at low compaction energy by a spoon, and definition of sedimentation height to identify uniform sedimentation and segregated sedimentation, and (b) consolidation test: automatic loading system and consolidometer for a sample of height H (2.54 mm) and diameter D (63.5 mm). Photo courtesy J. Jang.

Table 4
Representative correlations between compressibility coefficient, C_c (Table 8), and index properties (Table 6) of remolded fine-grained sediment. Note the liquid limit, plastic limit and plasticity index (LL, PL and $PI = LL\text{-}PL$, respectively) are all used here in units of %. They are measured with deionized water, but the specimens retained their in situ salt content and their behavior is influenced by that salt. G_s is the specific sediment density. The void ratio at the liquid limit, e_{LL}, is calculated via Eq. (1), with the water content, w_c, set to the liquid limit, LL.

Correlation	Reference
$C_c = 0.007 \cdot (LL - 10)$	Skempton and Jones (1944)
$C_c = 0.5 \cdot PI \cdot G_s$	Wroth and Wood (1978)
$C_c = .2343 \cdot e_{LL}$ $= .2343 \cdot (w_c \cdot G_s) = .2343 \cdot (LL/100) \cdot G_s$	Nagaraj and Murthy (1986)

first loading and unloading cycle. During the reloading cycle, the reservoir fluid salinity was changed as noted in the results for each specimen.

The consolidation test procedure started with preparing the specimen at a nominal 10 kPa of vertical stress, σ'. The stress was then increased by doubling in steps up to 2.560 MPa. This first loading process provides the compression index (C_c). The unloading procedure was to remove the load in two steps so the swelling index (C_s) could be obtained. The reservoir fluid was replaced, and we repeated the loading procedure to get the recompression index (C_r) and the unloading steps for C_s. The indices from the consolidation test are obtained by e-logσ' curve:

$$C_c,\ C_s,\ or\ C_r = -\frac{e_{1000kPa} - e_{100kPa}}{log1000kPa - log100kPa} \quad [2]$$

Because of limited sample volumes, two samples could not be consolidated: 3C-3P from UBGH2-3 and 6C-6P from UBGH2-6.

At each consolidation step, the hydraulic conductivity, K, was measured based on the consolidation theory approach from Terzaghi et al. (1996):

$$K = c_v \cdot m_v \cdot \gamma_w \quad [3]$$

The coefficient of consolidation, c_v, is derived from the decrease in void ratio with time during each consolidation step using Taylor's (1948) square-root time method. The coefficient of volume compressibility, m_v, is calculated from the change in stress, $\Delta\sigma$, and void ratio, Δe, at each consolidation step:

$$m_v = -\frac{\Delta e / \Delta \sigma}{1 + e_i} \quad [4]$$

and e_i is taken as the void ratio at the beginning of each step. The unit weight of water, γ_w, is taken as 9.8 kN/m^3. The permeability, k (mD, millidarcy = 9.87 × 10^{-16} m^2), is calculated from the hydraulic conductivity, K (m/s) according to:

$$k = \left(\frac{1}{9.87x10^{-16}}\right)\frac{K \cdot \zeta_w}{\rho_w \cdot g} \quad [5]$$

Assuming deionized water for the laboratory tests, we use a water viscosity, $\zeta_w = 1 \times 10^{-3}$ Pa s, water density, $\rho_w = 1000$ kg/m^3, and gravity, $g = 9.8$ m/s^2.

5. Results

This study focuses on how the permeability and compressibility of UBGH2 sites sampled would respond to methane gas hydrate dissociation and gas production, particularly with regard to sediment compressibility and permeability. We build on a series of "key takeaways" from our index property, sedimentation, liquid limit and 1D consolidation tests (Table 5). In this section, we describe how the measurement results shape our understanding of the compressibility and permeability behavior.

5.1. Sediment characterization

The UBGH2 sediment characterization is summarized in Table 6 (index properties), Table 7 (mineralogy), and Fig. 5 (sediment imagery). Based on grain size, sediment tested in this study is all classified as clayey silt according to the Wentworth classification scheme (Wentworth, 1922). Based on their liquid limit and plasticity index values, the samples are classified as elastic silt, designated as MH in the unified soil classification system (USCS, ASTM D2487 (ASTM, 2011a)). Fig. 5a and b shows that sediments clumped as they dried prior to being imaged, indicating the importance of electrical interactions in controlling the behavior of these fine-grained sediments.

As anticipated from in situ logging data (Bahk et al., 2013b), mineralogy data (Table 7) indicate diatoms are present in all samples studied here, and are particularly abundant in the samples from UBGH2-6B,C and the deepest UBGH2-3C sample. SEM imagery confirms diatoms are present, primarily as fragments, but with some specimens remaining largely intact (Figs. 1 and 5d,e). XRD mineralogy results confirm quartz, mica and feldspars are also significant sediment components at our test locations (Table 7), but diatoms play a critical role in determining the measured index properties. As measured by Jang et al. (2018), the internal porosity of the diatom structure (Zglobicka et al., 2017) leads to low specific density ($G_s = 2.23$) and high specific surface area ($S_s = 98$) relative to other sediment components. The diatom contents are high enough, particularly in the imaged UBGH2-3 and UBGH2-6 samples, to measurably reduce the specific gravity and dry weight of sedimentation test specimens (Table 6), but increase the specific surface area results relative to the specimens with lower diatom content.

Table 5
Key takeaways from the main experimental areas explored in this study.

Experimental area	Key result
Index properties	Low specific density and high specific surface results are consistent with diatom control of index properties
Imaging & mineralogy	Diatoms are abundant in the SEM imagery and from XRD, make up ~22–45% of the solid sediment by volume
Sedimentation	Rapid increase in sedimentation rate with even slight salinity increases is consistent with diatom control of sedimentation, resuspension and sediment fabric
Liquid limit	$LL_{DW} > LL_{2m,corr}$ is consistent with a void ratio increase due to pore-water freshening during production activities
1D compaction	Diatoms exert a more consistent control than do other minerals or index properties on compressibility
Permeability	Porosity and permeability preservation due to diatoms is observable in remolded specimens, but only for high diatom contents (>~45% by volume)

5.2. Sedimentation behavior

Fig. 6 shows sedimentation test results for UBGH2-2-2B 11H-4, UBGH2-3C 3P, UBGH2-3C 15P, and UBGH2-11B 16P. The sedimentation test results illustrate the free-fall, or sedimentation patterns of particles. The fine-grained sediment particles interact with each other and the pore fluid to form clusters, which can then settle. As the particles settle, the depositional height falls, and the accumulated sediment height increases (Fig. 4a). Clustering is controlled by the unbalanced surface charges on the particles and by the ionic concentrations in the pore fluid (Lambe and Whitman, 1969). Thus, the pore fluids affect the sedimentation results, and varying the pore-fluid chemistry yields information about which sediment components control the sedimentation behavior.

For all UBGH2 samples tested (Fig. 6, and for the mud interbed samples UBGH2-2-2B 15C, UBGH2-6B 18H-3C, and UBGH2-6C 6P, refer to Fig. 7 of Jang et al. (2020a)), the fine particles in the freshest water (DWF) stay suspended longer than in the more saline DWS. The DWF results are similar to the results of $(NaPO_3)_6$, the dispersant used to prevent clustering and subsequent settling. Sedimentation in DWS and 2 m-brine pore fluid behaves as expected when silica silt or diatoms are dominant (Fig. 8 in Jang et al. (2020a)). For silica silt and diatoms, even small ionic concentrations can reduce settling time by promoting fine particle clustering. The mica and illite content are nearly as high and sometimes higher than the diatom or quartz (silica) content, but mica and illite settle more rapidly as pore water freshens. If mica and illite were controlling factors in the UBGH2 sedimentation tests, the DWF and DWS sedimentation rates would be faster than the 2 m-brine sedimentation rates (open symbols in Fig. 6), but this is the opposite of what we observe. Since the sedimentation rates for the UBGH2 sites listed in Table 1 get faster as the salinity increases, we conclude the sedimentation is controlled by the diatoms and small quartz particles observed in the XRD mineralogy and SEM imagery.

5.3. Liquid and plastic limits

In this study, two liquid limit comparisons are of particular relevance: how liquid limit depends on salinity, and how liquid limit changes as a result of a compressibility test. As shown in Table 6, the liquid limit of each sample with deionized water (LL_{DW}) is greater than the liquid limit of the sample with 2 m brine ($LL_{2m,corr}$). This suggests the sediment fabric will seek to be more open as pore-water freshens during dissociation activities (higher void ratio, as indicated by Eq. (1)). Though consistent, these liquid limit differences are generally well below 10%, suggesting pore water salinity changes may not be the controlling factor for compressibility.

Liquid limit results shown parenthetically in Table 6 represent tests run on material that was used for a consolidation test prior to the liquid limit test. Samples UBGH2-3C 7P, 15P, and UBGH2-11B 16P show that

Table 6
Index properties of the UBGH2 specimens. Samples tested here are all classified as clayey silts according to their grain size (Wentworth, 1922), and as elastic silts according to their liquid limit and plasticity index values (ASTM, 2011a).

Type	Sample ID	d_{50} [μm]	G_s [ ]	LL [%]		*PL* [%]	*PI* [%]	S_s [m^2/g]	dry weight for Sedi. test [g]
				LL_{DW}: deionized water	$LL_{2m,corr}$: 2 m brine				
Fine-grained seal	2-2B 11H-4	5.1	2.664	64	63	32	32	39	7.06
Fine-grained interbed	2-2B 15C	5	2.664	66	61	–	–	40	7.49
	6B 18H-3C	5.7	2.523	110	92	57	53	52	3.79
	6C 6P	7	2.499	–	–	43	–	76	4.49
Fine-grained chimney sediment	3C 3P	8.5	2.507	–	–		–	30	7.28
	3C 7P	9.5	2.611	70 (60)[a]	(59)[a]	40	30	19	7.78
	3C 15P	7.5	2.460	79 (68)[a]	(60)[a]	44	35	42	7.02
	11B 16P	11	2.659	65 (54)[a]	(52)[a]	34	31	43	8.66

[a] LL tests after powdering the dry sample used for the consolidation test.

Table 7
XRD-based mineralogy results. Values are given in units of volume percent.

sample ID	2-2B 11H-4	2-2B 15C	6B 18H	6C 6P	3C 3P	3C 7P	3C 15P	11B 16P
quartz	16.7	16.6	10.4	12.1	17.5	23.7	20.5	18.4
opal-A (diatoms)	29.6	24.2	44.6	38.5	27.9	22.3	33.7	31.7
plagioclase	9.1	8.7	6.7	9.4	10.8	10.9	10.2	9.8
K-feldspar	7	6	7.1	7.1	5.1	7.1	5	5.1
micas (+illite)	32.7	34.6	24.8	27.1	22.5	23.9	25	29.1
kaolinite	3.4	3.8	2.5	2.8	2.9	3.3	2.9	3.6
smectite	1.5	1.5	1.5	1.7	0.6	1.1	0.7	1.1
calcite		3.6			7.5	5.4		
NaCl		1	2.4	1.3	5.2	2.3	2	1.2
total	100	100	100	100	100	100	100	100

LL_{DW} after consolidation is less than the initial LL_{DW}. This is a reminder that oven-drying (particularly at temperatures exceeding the 60 °C used in this study) can cause the sediment particles to aggregate, reducing *LL*, but also a reminder that increasing effective stress by even just a few MPa during the consolidation process can lower the resulting *LL* by crushing sediment components containing internal porosity, such as diatoms or other microfossils (Day, 1995; Shiwakoti et al., 2002).

5.4. 1D consolidation: compressibility

The primary measurement goals of this study are to establish the extent to which pore water salinity and diatoms control sediment compressibility and permeability so we can better constrain the sediment response to hydrate-related production activities at the selected Ulleung Basin sites. Table 8 and Fig. 7 show the consolidation test results. Table 8 provides the compression index (C_c), swelling index (C_s), and recompression index (C_r).

An important salinity consideration is that the tested samples are remolded, but still contain at least a portion of their in situ ions. As noted in the Methods section, the reservoir fluid in the consolidometer was initially DW, 0.6 m brine, or 2 m brine, then replaced with DW or 2 m brine after the initial loading and determination of C_c and C_s as shown in Table 8. Reservoir fluid replacement is a proxy for testing the effects of reservoir salinity changing over time, but as the series of three tests on UBGH2-2-2B 11H-4 show, salinity does not correlate with the compression indices. This result can be anticipated from the sedimentation results, in which even the small amount of pre-existing salt (DWS specimens) causes the tested sediments to behave as if they are in contact with brine. We therefore average the UBGH2-2-2B 11H-4 tests results and disregard the initial reservoir fluid type for the other samples when plotting the dependence of compressibility on various parameters. We take the compressibility results in this study as representative of the sediment in the presence of brine.

Representative correlations between index properties and the compressibility index, C_c, are given in Table 4. Comparisons between measured and predicted C_c values are plotted in Fig. 8. For $C_c < 0.45$, the correlations are generally consistent with the measured results. In this lower C_c range, we would recommend the void ratio correlation, which accounts for both the liquid limit and specific gravity of the soil. The correlations are empirical relationships that were not specifically developed for diatom-rich sediment, and as shown in Fig. 8, they significantly overpredict the measured results if C_c exceeds ~0.45. These correlations are meant for remolded clays in general, but the specific compositions of these UBGH2 samples contain high enough diatom concentrations to alter the expected compressibility.

Sediment compressibility depends on both the sediment constituents, and on how those constituents are arranged. Here, since we work with remoulded specimens, we assume the sediment components are distributed homogeneously and focus on the contribution from each sediment component. Specifically, we are interested in whether any component appears to provide a significant control on the overall sediment compressibility. Fig. 9 relates compressibility to the primary sediment constituents. Below $C_c \approx 0.45$, there are clear trends between the sediment content and compressibility. The open symbols track low compressibility components ($C_{c,component} < C_{c,sample}$). If any of these components were the primary control on compressibility, we would expect C_c to fall as the component fraction increased, but we observe the reverse. The filled circles are primarily for mica, $C_c = 0.86$ in brine, though XRD results for mica will also contain a contribution from illite, $C_c = 0.35$ (compressibilities from Jang et al. (2018)). Given the high compressibility for mica, we would anticipate C_c should decrease as the mica content falls, but again we observe the reverse. Note that if the illite contribution to the mica + illite component is significant, the general trend for mica + illite would be consistent with some illite control on the overall compressibility. Diatoms (red stars in Fig. 9) are both highly compressible ($C_c = 0.54$ in brine, Jang et al. (2018)) and the overall sample compressibility increases with increasing diatom content. It is unclear why the apparent diatom content for $C_c = 0.45$ (UBGH2-3C 7P) is so low, but overall, diatoms are the primary constituent (volume fraction exceeding 5%) for which the overall compressibility trend with composition responds as anticipated given the constituent compressibility.

The swelling index, C_s, and recompression index, C_r, values do not change significantly when the reservoir fluid is changed between the first and second consolidation cycles. Taken together, our results suggest the compressibility of the remolded samples is dependent on the particle morphology and mineralogy, but the pore fluid chemistry barely affects the recompression and swelling of the samples after virgin compression.

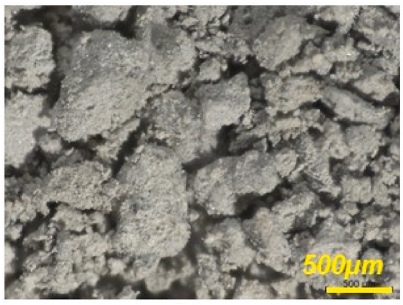

(a) UBGH2-2-2B 11H-4

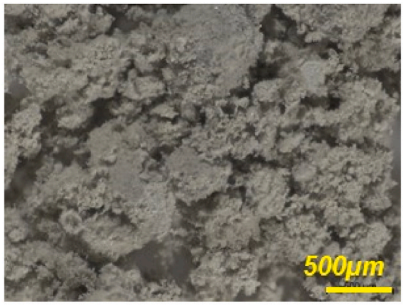

(b) UBGH2-6B 18H-3C

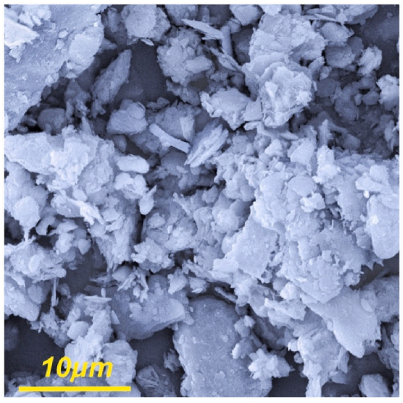

(c) UBGH2-2-2B 11H-4

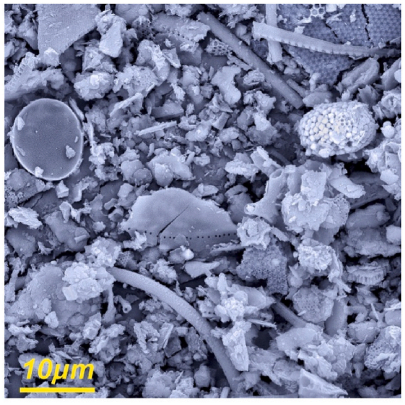

(d) UBGH2-6B 18H-3C

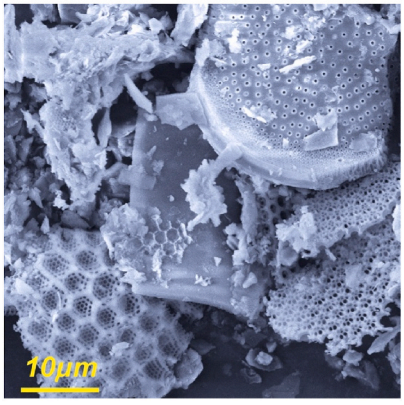

(e) UBGH2-3C 15P

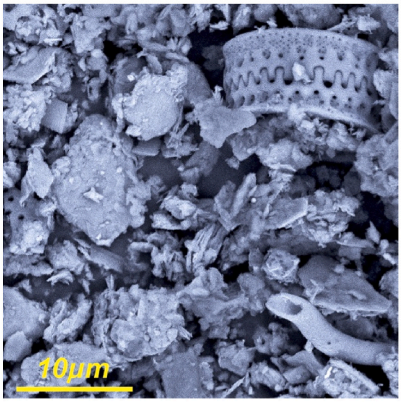

(f) UBGH2-11B 16P

Fig. 5. Microscopic images and SEM images for particle morphology: (a) and (b) are microscopic images of reservoir-element mud (UBGH2-2-2B 11H-4) and seal-element mud interbeded between sand layers (UBGH2-6B 18H-3C); (c) and (d) are SEM images of the same two samples; (e) and (f) are SEM images of fine-grained sediment associated with methane hydrate bearing sediments in a chimney. Diatoms and diatom shards are abundant in (d), (e) and (f), and see also Fig. 1 for examples of diatom and diatom shard morphologies. Framboidal pyrite is also commonly found in these samples; one example is the oval cluster of small, white crystals in the upper right quadrant of (d).

5.5. Permeability

The coefficient of consolidation, c_v, coefficient of volume compressibility, m_v, effective stress, σ, void ratio, e, porosity, n, hydraulic conductivity, K and permeability, k, are all available digitally (Jang et al., 2022a). Here we focus only on permeability, specifically how diatoms alter the dependence of permeability and porosity on effective stress (Fig. 10). Specimen UBGH2-2-2B 11H-4 was tested three times, each with a different pore-fluid chemistry profile (indicated in Table 8). There is no correlation between the permeability and the pore fluid chemistry, suggesting that as with the sedimentation and compressibility results, the existing salinity in the specimen causes the sediment to behave as if it is in contact with a brine. Full results for UBGH2-2-2B 11H-4 are given in Fig. 13b, but for clarity in comparing between sites, only the deionized water results are presented in Fig. 10.

To illustrate the role diatoms play in determining porosity and permeability, we compare the UBGH2 results with the consensus porosity and permeability measured via consolidation theory as well as direct fluid flow on a fine-grained seal sediment sample from above a gas hydrate reservoir offshore India at NGHP-02-08 (Dai et al., 2019; Jang et al., 2019a; Priest et al., 2019). The NGHP-02-08 specimen (star in Fig. 10) did not appear to have diatoms (Jang et al., 2019a), but did have a comparable grain size, d_{50} = 7.9 μm, and an even higher specific surface, S_s = 278 m^2/g (Dai et al., 2019) than the UBGH2 specimens studied here. Given the NGHP02-08 grain characteristics (absence of diatoms, small grain size and high specific surface) the permeability at a given porosity could be expected to be lower than the diatom-rich specimens from UBGH2, but this is not what we observe.

Porosity preservation due to diatoms for these remolded specimens is particularly evident for the highest diatom content sample (UBGH2-6B

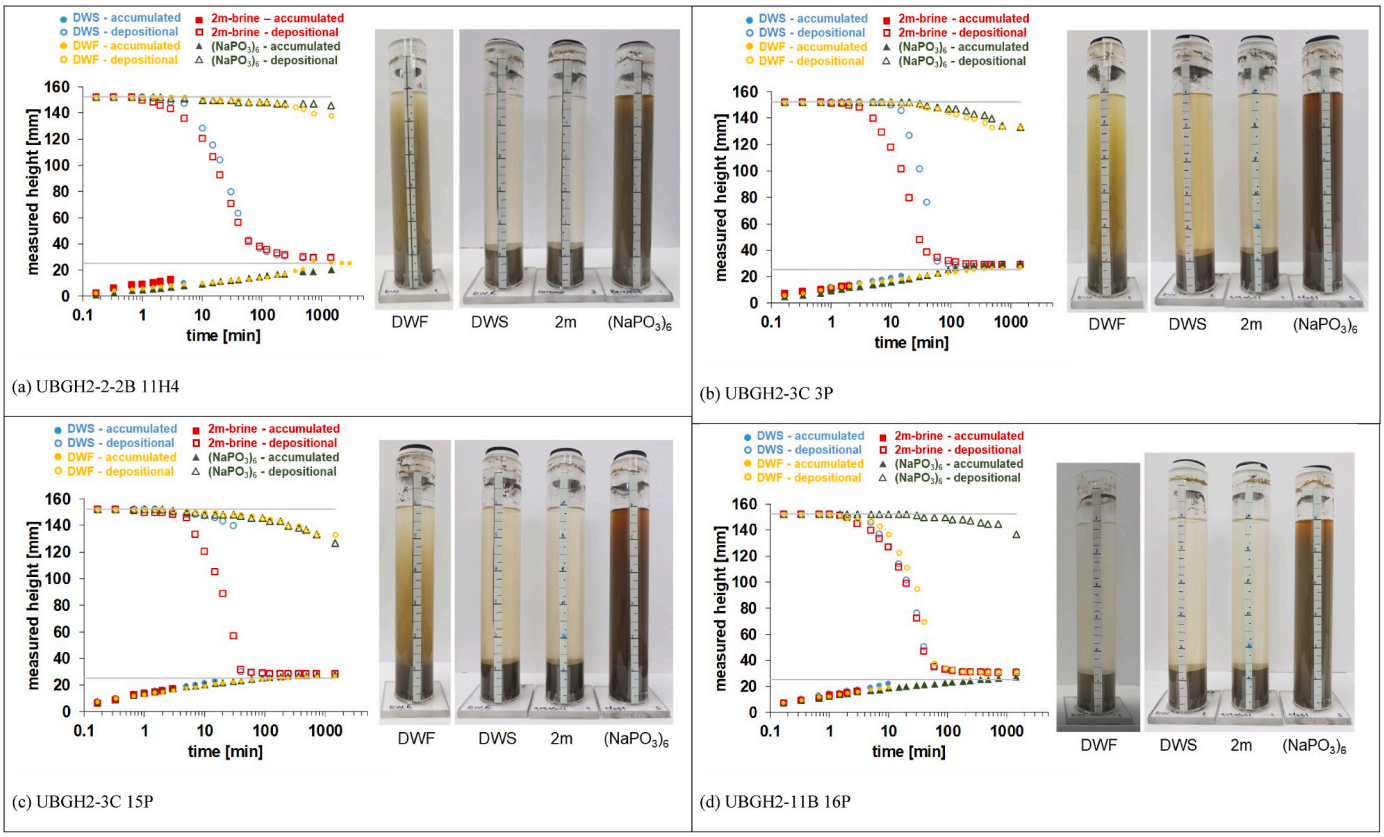

Fig. 6. Sedimentation test results in deionized water (DWS), diluted DWS (DWF), 2 m brine (2 m), and $(NaPO_3)_6$ solution. The upper gray line in the graphs is 152.4 mm as the fluid column and lower gray line in the graphs is 25.4 mm, the loosely-packed height. Sedimentation data can be downloaded from Jang et al. (2022b).

Table 8
Compression index, swelling index and recompression index from 1D consolidation tests. Specimens 6C 6P and 3C 3P did not contain enough sediment to complete these tests and are listed as not applicable (N/A).

Type	Sample ID	Ionic concentration (IC)	loading		reloading	
			loading	unloading	reloading	unloading
		loading→reloading	C_c	C_s	C_r	C_s
Fine-grained seal	2-2B 11H-4	0.6 m → DW	0.439	0.13	0.08	0.09
		2 m → DW	0.40	0.07	0.11	0.08
		DW → 2 m	0.37	0.07	0.12	0.07
Fine-grained interbed	2-2B 15C	2 m → DW	0.36	0.08	0.11	0.07
	6B 18H-3C	2 m → DW	0.56	0.13	0.09	0.09
	6C 6P	N/A				
Fine-grained chimney sediment	3C 3P					
	3C 7P	0.6 m → DW	0.45	0.09	0.08	0.06
	3C 15P	0.6 m → DW	0.44	0.06	0.12	0.07
	11B 16P	0.6 m → DW	0.425	0.07	0.11	0.08

18H-3, 44.6% diatom content), which was able to retain a porosity of 58% at the peak effective stress of 2.56 MPa. At this stress, the remaining specimens, with diatom contents ranging from 22 to 34% are all consistent with, or more porous than, the NGHP02-08 sample (Fig. 10a). The elevated UBGH2 porosity does not equate with elevated permeability, however. As shown in Fig. 10b, the diatom-free NGHP02-08 sediment permeability (0.02 mD at 2 MPa effective stress) is consistent with or higher than all of the measured UBGH2 permeabilities measured at ~2.5 MPa, and higher than all but UBGH2-6B 18H-3 results measured at ~ 1.1 MPa. Results shown in Fig. 10 indicate the presence of diatoms alone does not guarantee an elevated permeability, even when the diatom content is above ~45%. Though diatoms and diatom shards provide additional pore space thanks to their jagged, porous structures (Figs. 1 and 5), the low permeability results indicate connectivity between those pore spaces is restricted by narrow openings in the diatoms (e.g., Fig. 1b "inner porosity") and/or increased fluid pathway tortuosity through enmeshed, interlocking shards (e.g., Fig. 5e).

6. Discussion

To better understand how our laboratory results apply to the in-situ environment, it is useful to summarize the conclusions from Shiwakoti et al. (2002), who specifically tested how remolding altered the properties of diatom-rich sediment. Two of their key conclusions are: 1) when mixed into the fine-grained host sediment (they used kaolin), diatom contents of 30% (by volume) are sufficient to significantly enhance both the compressibility (40% increase) and permeability (factor of 2 increase), and 2) the remolding process can break silica

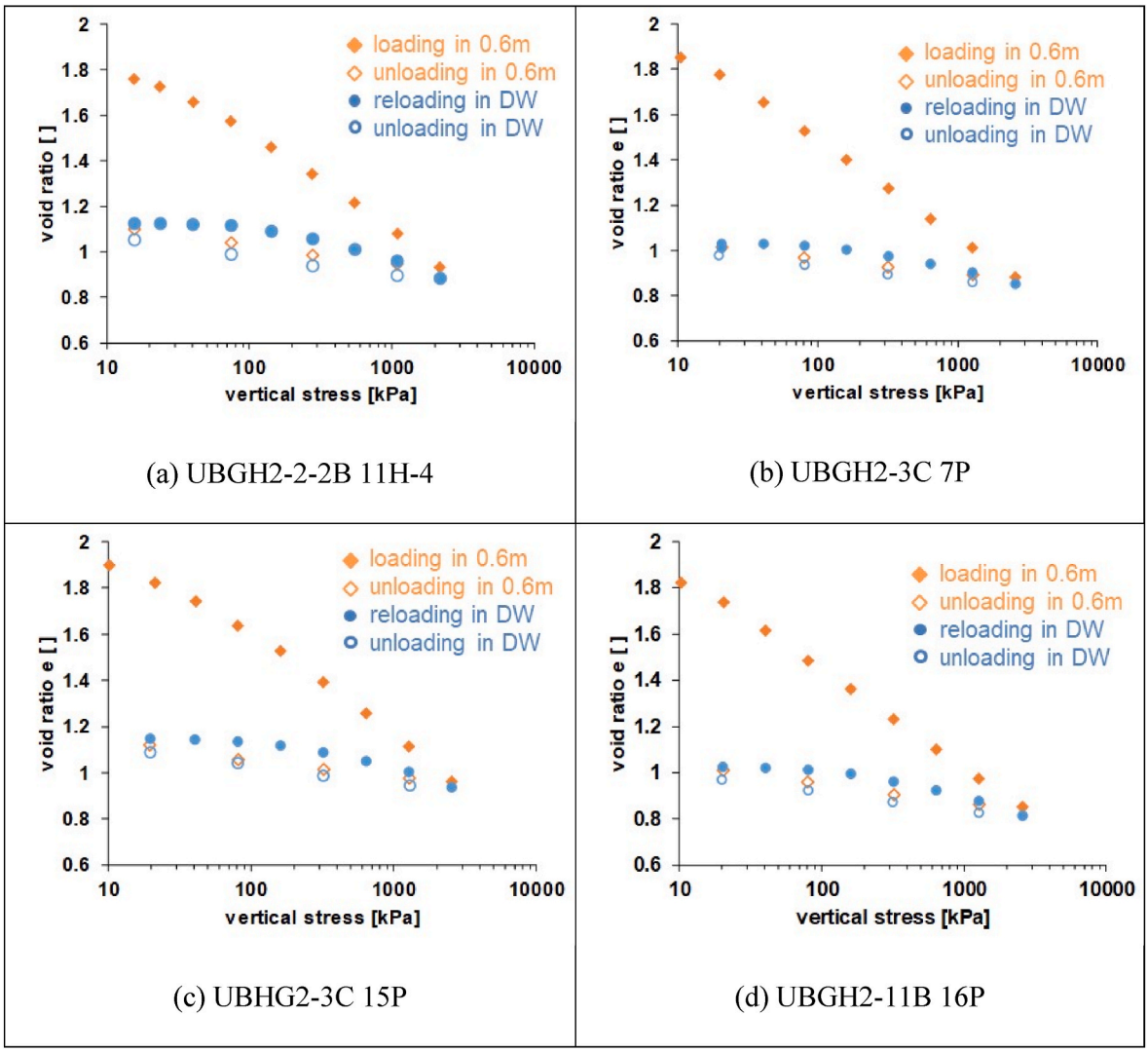

Fig. 7. 1D incremental loading consolidation of UBGH2 samples. For the tests shown here, each sample was initially mixed with deionized water at $1.2LL_{DW}$. The water reservoir of the consolidometer was initially 0.6 m brine, then replaced with deionized water after the first loading and unloading sequence. The complete set of consolidation data can be downloaded from Jang et al. (2022a).

bonds that may have formed between diatoms in addition to breaking a fraction of the diatoms themselves. The resulting sediment void space reduction reduces the sediment's compressibility and permeability (Shiwakoti et al., 2002). Their results indicate that even though compressibility and permeability results reported here (diatom contents ranging from ~22 to 44% by volume, Table 7), are likely to be higher than if the sediment had been diatom-free, the results for undisturbed in situ material should be even higher than our observations and our compressibility and permeability results should be taken as lower bounds for the in situ properties.

6.1. Production from layered gas hydrate systems (e.g., UBGH2-2, UBGH2-6)

Here we look at how properties of the diatom-rich sediment studied here could impact the extraction of methane from hydrate via depressurization of hydrate-bearing sediment. Figs. 11 and 12 display the logging-while-drilling (LWD)-based estimates of gas hydrate saturation at UBGH2-2-2B and UBGH2-6B. The highly variable hydrate saturation is indicative of the layered gas hydrate system composed of highly hydrate-saturated, generally coarse-grained layers separated by finer-grained interbed layers. The hydrate-bearing layers are more vertically-distributed at UBGH2-2-2B than UBGH2-6B, but conceptually they offer similar environments in which to examine the significance of diatom-rich sediment on production performance. We use UBGH2-6B for our numerical examples, since it is a potential production test site (Ryu et al., 2013).

Boswell et al. (2019) note that for hydrate reservoirs beneath water depths exceeding 2000 m (Table 1), significant pore-pressure drawdowns are required to destabilize gas hydrate and liberate the methane. To establish the minimum pressure drawdown that would destabilize gas hydrate, we need to know the in situ hydrostatic pressure as well as the hydrate stability pressure at the in situ temperature. The in situ hydrostatic pressure, P_{hydro}, is given by:

$$P_{hydro} = \rho_{seawater} \cdot g \cdot (water\ depth + depth\ below\ seafloor) \quad [6]$$

where we use a seawater density, $\rho_{seawater} = 1030\ kg/m^3$ and gravity, $g = 9.8\ m/s^2$. For UBGH2-6B, the water depth is 2154.2 m (Table 1) and the primary gas hydrate-bearing sediment layers (Fig. 12) are between 140 and 155 m below seafloor (mbsf). Taking 150 mbsf as an example, the in situ hydrostatic pressure is 23.3 MPa.

The in situ reservoir temperature, $T_{reservoir}$, is calculated from the geothermal gradient, 0.112 °C/m, and bottom water temperature, 0.48 °C (Ryu et al., 2013), according to:

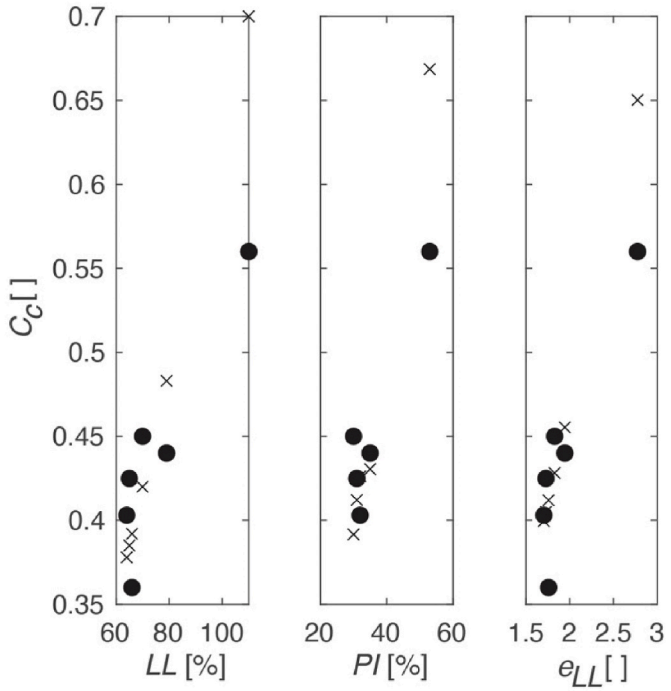

Fig. 8. Compressibility coefficient, C_c, correlations with liquid limit, *LL*, plasticity index, *PI*, and the void ratio at the liquid limit water content, e_{LL}. Measured data are given by solid circles (Table 8). Correlations derived from the equations in Table 4 and values given in Table 6 are given by crosses. Below $C_c \approx 0.45$, the correlations are generally consistent with the data, but significantly overpredict the $C_c = 0.56$ result (UBGH2-6B-18H-3C). Compressibility data can be downloaded from Jang et al. (2022a).

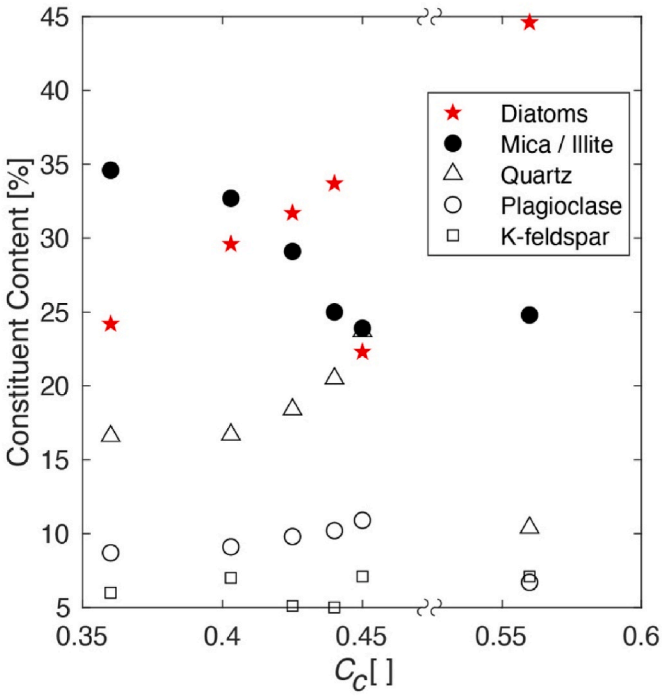

Fig. 9. Compressibility coefficient, C_c (Table 8), dependence on mineralogy (Table 7). Open symbols represent sediment components that are less compressible than the samples measured here. Increasing their concentration should decrease the overall compressibility, but we observe the opposite trend. The solid symbols represent sediment components that are generally more compressible than the samples measured here, so increasing their concentration should increase the overall compressibility. This trend holds only true for diatoms (red stars), suggesting diatoms provide a critical control on the compressibility of these UBGH2 sediments. (For interpretation of the references to colour in this figure legend, the reader is referred to the Web version of this article.)

$$T_{reservoir} = 0.48^{\circ}\mathrm{C} + 0.112^{\circ}\mathrm{C/m}\cdot \textit{depth below seafloor} \quad [7]$$

or 17.28 °C for UBGH2-6B at a reservoir depth of 150 mbsf. Using the hydrate stability curve provided by Tishchenko et al. (2005) for seawater with a typical 35 parts per thousand salinity, the reservoir's hydrostatic pressure must be reduced from the in situ value of 23.3 MPa to below 20.4 MPa for hydrate to destabilize. This ~3 MPa pore pressure decrease generates an additional 3 MPa effective stress on the sediment. Kim et al. (2013b) indicates the in situ effective stress is ~0.9 MPa for the UBGH2-6B gas hydrate reservoir, meaning an overall effective stress of at least ~4 MPa will be imposed during the depressurization process. A maximum anticipated effective stress during depressurization, 15 MPa, is suggested by Kim et al. (2017) in a review of reservoir parameters required for modeling production from UBGH2-6B.

Figs. 11 and 12 compare the compressibility values measured here on remolded samples with the compressibility results from Kim et al. (2013b) and Lee et al. (2013a). The sample depths are given relative to the LWD profiles for UBGH2-2-2 and UBGH2-6. It can be difficult to know if data from a particular depth correspond to a coarse-grained reservoir or a fine-grained interbed layer, but all C_c results plotted here are taken from the very fine-grained samples ($d_{50} < 12.5$ μm) characteristic of interbeds or overlying seal material. For comparison, Bahk et al. (2013a) report the average grain size for the UBGH2 reservoir sands is 134 μm.

As anticipated from the work of Shiwakoti et al. (2002), compressibilities for the remolded specimens (red stars in Figs. 11 and 12) are lower bounds for the compressibility of undisturbed or minimally-disturbed sediment (open symbols in Figs. 11 and 12). In comparison to the fine-grained seal and interbed sediment tested here, the compressibility of the coarser reservoir sediment is low, measured by Kim et al. (2017) to be $C_c = 0.207$. Table 8 and Fig. 8 show the diatoms present in UBGH2-2-2 and UBGH2-6 sediment contribute to measured sediment compressibilities that are ~70–170% higher than the nominal reservoir compressibility, and based on the Shiwakoti et al. (2002) conclusions, this difference should be even greater when considering in situ, undisturbed sediment. This result is consistent with the properties of diatoms. Diatoms are highly compressible (Jang et al., 2018) because the diatoms themselves are easily crushed as effective stress increases above 200–350 kPa, leading to dramatic porosity reductions (Shiwakoti et al., 2002). High compressibility sediments can be a liability during a depressurization-style production because the compressing or subsiding sediment imparts stress on the well casing itself, which can fail either in tension or in compression depending on how stress from the compacting sediment gets distributed along the well walls (Hancock et al., 2019).

A second production liability diatoms can contribute to is in the permeability of sediments bounding the gas hydrate reservoir. Where diatom abundance is high enough to preserve elevated porosity and permeability in the seal sediment overlying a reservoir, such as in Area B offshore India (Jang et al., 2019b), reservoir depressurization becomes less efficient due to water migrating from the permeable "seal" sediment into the reservoir during depressurization (Jang et al., 2020b). Reservoir modeling by Ajayi et al. (2018) and Konno et al. (2019) demonstrate the importance of seal sediment permeability when modeling the reservoir production efficiency. As Ajayi et al. (2018) point out for a permafrost-associated gas hydrate reservoir on the Alaska north slope, the predicted production efficiency drops by a factor of two when considering a seal with 1mD-permeability rather than the idealized zero-permeability seal.

Fig. 10 indicates that even with the diatom contents observed in these UBGH2 specimens, the permeability is quite low. The results for

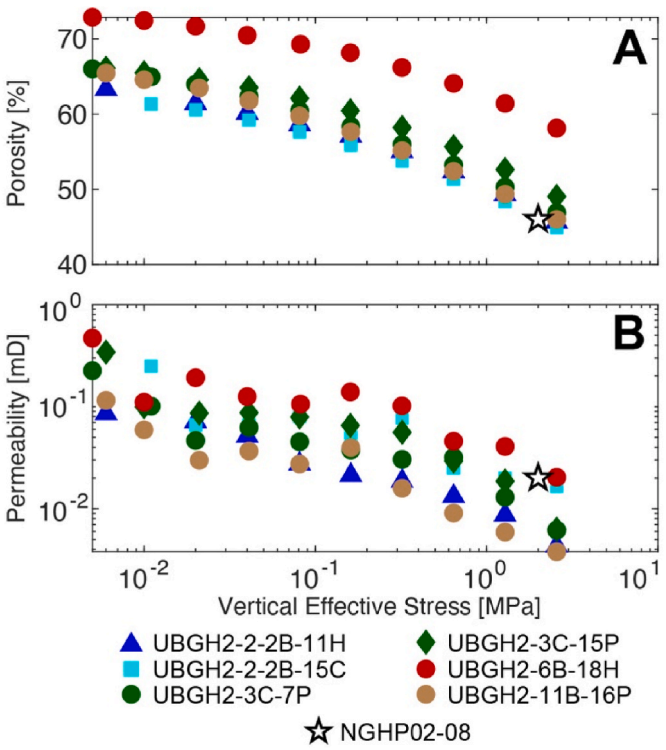

Fig. 10. (a) Porosity and (b) permeability dependence on vertical effective stress. Solid symbols represent measured results from each consolidation step. The two highest diatom-content samples (UBGH2-6B-18H, red circle with 44.6% diatoms by volume, and UBGH2-3C-15P, green diamond with 33.7% diatoms by volume) preserve the most porosity with increasing effective stress, but porosity does not correlate well with lesser diatom contents. Permeability is less dependent on diatom content, though the highest diatom content does generally yield the highest permeability. The star is a consensus result (46% porosity, 0.02 mD, 2 MPa effective stress) for an essentially diatom-free seal sediment sample above a gas hydrate reservoir offshore India at NGHP-02-08 (Jang et al., 2019a, see also Dai et al., 2019 and Priest et al., 2019). UBGH2 results at a similar effective stress generally show equivalent or larger porosities, yet lower permeability, indicating the presence of 22–34% diatoms by volume in these remolded UBGH2 samples does not guarantee higher permeability relative to diatom-free sediment. UBGH2 data are available for download (Jang et al., 2022a). (For interpretation of the references to colour in this figure legend, the reader is referred to the Web version of this article.)

UBGH2-2-2B and UBGH2-6B are consistent with the measurements of Kim et al. (2013b), which were also made via the Terzaghi et al. (1996) consolidation theory (Eq. (3)) (Fig. 13). Like the data measured here, Kim et al. (2013b) measured permeability as they increased the applied effective stress, so the points toward the lower left in each plot represent porosity and permeability at the highest applied effective stress (~1.8 MPa). Kim et al. (2013b) note the in situ effective stress for UBGH2-6B is approximately 0.9 MPa, and three points from their study that are representative of in situ permeability at that effective stress for the overlying seal, OS, the interbedded fine-grained layers, IL, and underlying seal, US, are highlighted in Fig. 13b.

Taking the data from both sites together, the in situ permeability is likely to be on the order of 0.01mD. Even the highest diatom-content specimen, UBGH2-6B 18H-3C (red circles in Fig. 13b), has a permeability of only ~0.04mD at an effective stress of 0.9 MPa. For comparison, the hydrate-free reservoir sediment has an intrinsic permeability of ~180mD (Kim et al., 2017), four orders of magnitude higher than that of the fine-grained sediment. In the presence of gas hydrate (S_h = 65%), Kim et al. (2017) suggests the reservoir permeability will be ~3mD, which is still two orders of magnitude more than the expected in situ permeability in the fine-grained seals and interbeds.

Even at their in situ, undisturbed permeabilities, the seal and interbed sediments are likely to behave as effective seal sediments for production. Compaction during production will further decrease the porosity and permeability in these compressible fine-grained layers, particularly if pressure drawdowns of 15 MPa are applied as suggested by Kim et al. (2017). Such an increase is approximately eight times the maximum effective stress applied to get the data points shown in Fig. 13, so permeabilities in the fine-grained sediments could decrease to the order of microdarcies during production. In spite of the observed diatom content in the fine-grained seal and interbed sediments, these sediments appear to be able to provide effective seals during production. Based on sedimentation and liquid limit results showing the sediment's sensitivity to even low salinity, we do not believe the compressibility and permeability response to depressurization will change as the pore water freshens due to gas hydrate dissociation during production.

Even if the seals and interbed are effective at limiting fluid flow into the reservoir sediment during production, the presence of diatoms in the fine-grained layers could present a challenge to the long-term permeability of the reservoir itself. Thinly-layered gas hydrate reservoirs subjected to depressurization likely have preferential hydrate dissociation at the interfaces between reservoir layers and the fine-grained interbed or bounding seal sediments due to the fine-grained layer's capacity to provide heat to sustain the endothermic dissociation of gas hydrate (Myshakin et al., 2019). The sediment motion modeling by Uchida et al. (2019) demonstrates how this preferential gas hydrate dissociation can mobilize sands from the interfaces between reservoir and interbed/seal sediment, entraining sand particles in the fluid flow toward the production well. Oyama et al. (2016) show that the fluid flow rates required to mobilize fine-grained particles are an order of magnitude smaller than what is required to mobilize the coarse grains, meaning the preferential hydrate dissociation will likely erode the fine-grained layers, drawing fine-grained particles into the fluid flow toward the well. Jang et al. (2020a) point out that diatoms and diatom fragments in UBGH2 sediments are particularly prone to clogging pore throats, especially in systems with mixed gas and fluid flow in which the fluid/gas meniscus concentrates the fine-grained particles entrained in the flow (Cao et al., 2019). Permeability reduction due to reservoir pore-throat clogging at or near the well bore reduces the overall well production efficiency and will be exacerbated by diatoms detached from the interbed and seal layers.

6.2. *Production from chimney gas hydrate systems (e.g., UBGH2-3, UBGH2-11)*

Sites UBGH2-3 and UBGH2-11 are representative of fine-grained chimney environments. Chimney structures have long been viewed as conduits for enhanced fluid and gas flow, promoting gas hydrate growth by supplying methane-rich fluid (or gas) into the hydrate stability zone (e.g., Anderson and Bryant, 1990; Hyndman and Davis, 1992). As shown in Fig. 3, these chimneys can have massive gas hydrate near the seafloor above a deeper network of gas hydrate filled lenses, and diatoms can act to promote the formation of these hydrate morphologies. As noted previously, diatoms can provide pore spaces that are larger than in the surrounding fine-grained sediment, allowing hydrate to form at lower pore-water methane concentrations than is possible in small pores (Kraemer et al., 2000). Once formed, gas hydrate can then grow beyond the limits of the diatom-rich layer and into the surrounding fine-grained sediment via fracture formation and fill (Daigle and Dugan, 2010; Oti et al., 2019). Near the seafloor, hydrate growth in chimneys can even generate massive, nearly sediment-free gas hydrate (see imagery from UBGH2-7 in Ryu et al., 2013; offshore western Japan in Matsumoto et al., 2017; Yoneda et al., 2019a; and from the South China Sea in Ye et al., 2019).

The resource potential of near-seafloor, massive gas hydrate is not yet well understood (Matsumoto et al., 2017), and currently the most economically-viable gas hydrate morphology to target is thought to be

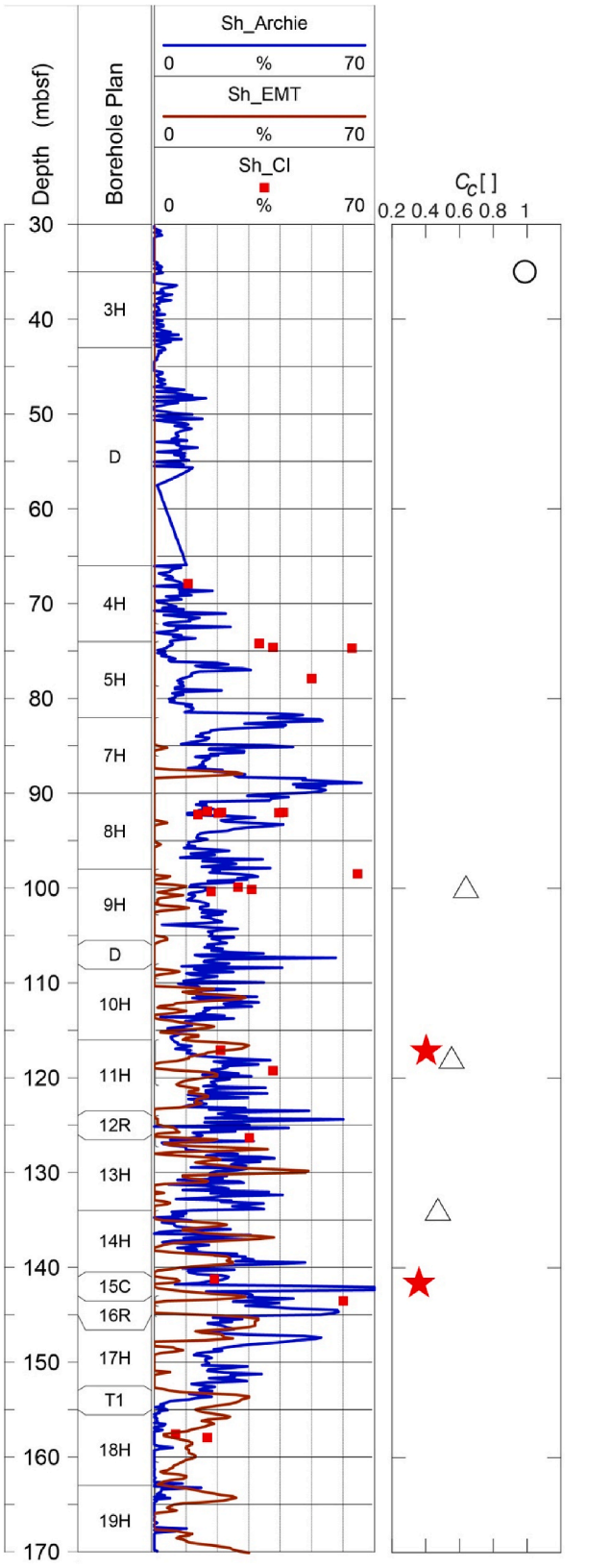

(caption on next column)

Fig. 11. Sediment compressibility profile with depth for UBGH2-2-2B. Downhole depth, borehole plan and log display are adopted from Bahk et al. (2013b). Here we show hydrate saturations profiles derived by applying Archie's Law (Archie, 1942) to logging-while-drilling (LWD) measurements from the ring resistivity tool, S_h*Archie*, by applying the effective medium modeling approach of Helgerud et al. (1999) to the LWD velocity tool data, S_h*EMT*, and from core measurements of pore-water chlorinity anomalies (Kim et al., 2013d), S_h*Cl*. The borehole plan (Bahk et al., 2013b) indicates core numbers, or "D" for a drilling interval and "T1" for a downhole temperature measurement. UBGH2-2-2B is a thinly-layered gas hydrate reservoir, as indicted by the narrow spikes of high gas hydrate saturation. Compressibility data measured on remolded sediment for this study (solid stars, Table 8) represent lower bounds for the compressibility of undisturbed, in-situ sediment. As expected, compressibilities measured on minimally-disturbed recovered core (open triangles, Kim et al. (2013b); open circle, Lee et al. (2013a)) exceed the remolded values.

gas hydrate in coarse-grained sediments that can be destabilized via depressurization (e.g., Yamamoto et al., 2017). Depressurization is not considered a viable option for recovering methane from predominantly fine-grained environments due to low initial permeability of the host sediments (Moridis and Sloan, 2007; Jang and Santamarina, 2016b). Boswell and Collett (2011) note the vast majority of gas hydrate is hosted in fine-grained sediment, however, and Zhang et al. (2020) suggest certain fine-grained environments, such as chimney structures with porosity preservation due to skeletal fragments in the sediment, may have enough fluid flow and available pore space to merit assessment as hydrate-based energy resources. Here we discuss the implications of diatoms on three proposed production strategies: horizontal wells, direct removal of the hydrate and host sediment, and extraction of methane in the hydrate via replacement in the hydrate structure by carbon dioxide, CO_2.

Mao et al. (2021) show horizontal wells can improve resource extraction efficiency, in part by increasing the area over which the well contacts a hydrate-rich layer. For chimney environments, however, gas hydrate tends to occur in isolated sand bodies of limited spatial extent as noted for site UBGH2-11 (Lee et al., 2013b) or as grain-displacing, hydrate-filled veins at both UBGH2-3 (Lee and Collett, 2013; Lee et al., 2013b) and UBGH 2-11 (Lee et al., 2013b). The limited spatial extent of these hydrate-rich bodies reduces the contact area horizontal wells can attain with hydrate, but horizontal wells, or multiple angled wells, do have the potential to contact many hydrate-filled veins and more effectively extract methane from fine-grained sediment (Ning et al., 2022).

One approach that capitalizes on a well that contacts many hydrate-filled veins is the fluidization approach. In fine-grained sediment offshore China, Liu et al. (2019) report on the effectiveness of fluidizing the hydrate and sediment around the well, then pumping both the hydrate and sediment to the surface for separation and processing. High diatom concentrations in the UBGH2 environments can further benefit the fluidization process by lowering the sediment density, thereby lowering the demand on the pumps (e.g., Table 7: diatom concentrations between 22 and 34%; Table 6: $G_s < 2.66$ for UBGH2-3 and UBGH2-11).

Fluidization destroys the mechanical integrity of the reservoir, which may not be acceptable in all situations. To preserve the reservoir's mechanical stability, methane extraction via direct replacement of methane by carbon dioxide (CO_2) in the hydrate has been proposed. Theoretical (Dornan et al., 2007) and laboratory (Park et al., 2006) results show it is energetically favorable for CO_2 (and a carrier gas such as nitrogen) to replace methane in the hydrate structure. This replacement process happens spontaneously, though high replacement rates strongly depend on large interfacial contact areas between the invading CO_2 and the original methane hydrate (Schicks et al., 2011). This spontaneous

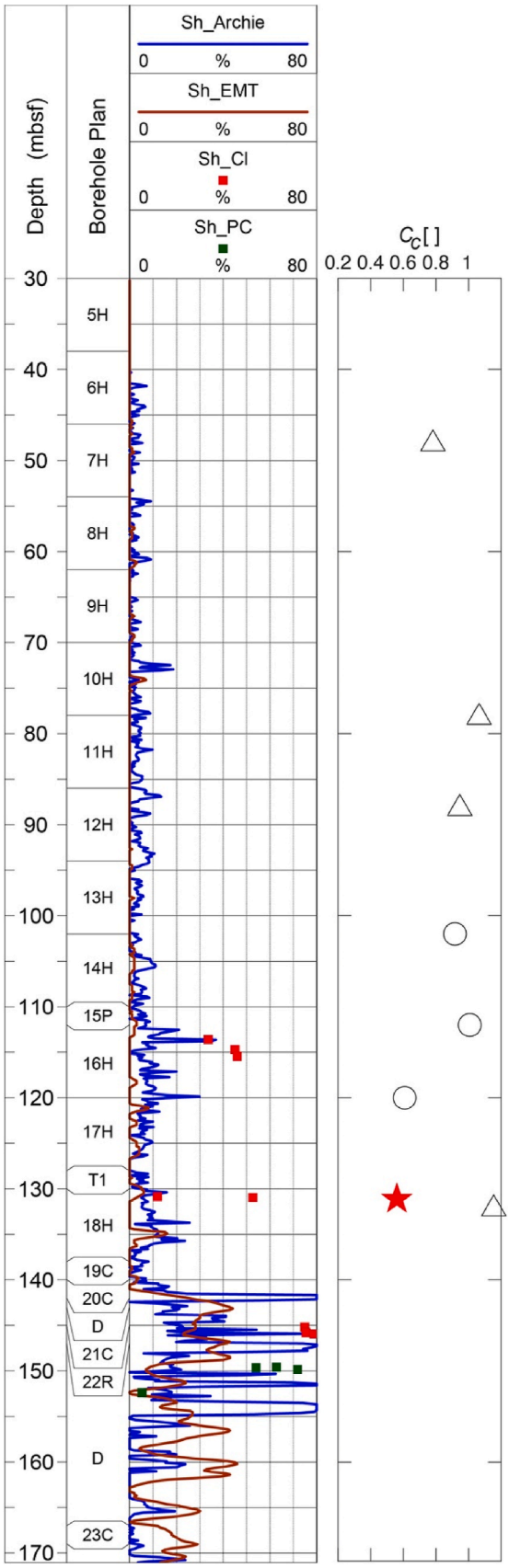

(caption on next column)

Fig. 12. Sediment compressibility profile with depth for UBGH2-6. Downhole depth, borehole plan and log display are adopted from Bahk et al. (2013b). In addition to hydrate saturations profiles derived from the LWD the ring resistivity data, S_h*Archie*, from LWD velocity data, S_h*EMT*, and core measurements of pore-water chlorinity anomalies, S_h*Cl* (See Fig. 11 for details), the hydrate saturations measured by degassing pressure cores, S_h*PC* are shown (green squares in the log display). Bahk et al. (2013b) display all of the S_h core data as chlorinity-based, but Kim et al. (2017) correctly differentiate between the chlorinity data (shown here as red squares), and data obtained from mass-balance calculations as hydrate-bearing pressure cores are degassed and their produced methane volumes measured (green squares). The borehole plan (Bahk et al., 2013b) indicates core numbers, or "D" for a drilling interval and "T1" for a downhole temperature measurement. Compressibility data measured on remolded sediment for this study (solid star, Table 8) again represents the lower bound for the compressibility of undisturbed, in-situ sediment. As expected, compressibilities measured on minimally-disturbed recovered core (open triangles, Kim et al. (2013b); open circles, Lee et al. (2013a)) exceed the remolded values. Like UBGH2-2-2, UBGH2-6 is a thinly-layered gas hydrate reservoir, as indicted by the narrow spikes of high gas hydrate saturation. (For interpretation of the references to colour in this figure legend, the reader is referred to the Web version of this article.)

replacement process was demonstrated in the Ignik Sikumi coarse-grained gas hydrate reservoir (Schoderbeck et al., 2013; Anderson et al., 2014; Schicks et al., 2018), and has been proposed for use on thin gas hydrate occurrences in fine-grained sediment (Jang and Santamarina, 2016b; Li et al., 2018).Where the presence of diatoms increases the permeability of undisturbed fine-grained host sediment, diatoms would benefit initial efforts to disperse CO_2 (likely with nitrogen as a carrier gas as was done at Ignik Sikumi (Anderson et al., 2014; Schicks et al., 2018)). Recovering methane released as the hydrate takes on CO_2 requires drawing fluid and gas into the production well, however. As described in Section 6.1, diatoms can be dislodged from the fine-grained host sediment, entrained in the production flow, and promote clogging at and near the production well, even for low diatom concentrations in the entrained flow (Cao et al., 2019; Jang et al., 2020a). Diatom entrainment and clogging is exacerbated by the reservoir geometry. The thin hydrate occurrences and the concentration of CO_2 replacement along the hydrate interfaces with the host sediment (Li et al., 2018) creates a similar arrangement as described in Section 6.1: methane and fluid flow back to the production well will be focused along the hydrate/sediment interfaces, increasing the fluid flow rate along these interfaces (Uchida et al., 2019), thus boosting the likelihood of entraining diatoms in the flow. Moreover, as methane bubbles move to the production well, the mobile gas/fluid menisci are particularly effective at entraining fines, including diatoms, concentrating the fines and promoting clogging (Cao et al., 2019; Jang et al., 2020a).

6.3. Conventional hydrocarbon production from beneath chimney gas hydrate systems (e.g., UBGH2-3)

Site UBGH2-3 is associated with the nearby Donghae-1 commercial gas field (Ryu et al., 2013), so there is the potential for extracting conventional hydrocarbons underlying the UBGH2-3 hydrate or from beneath similar chimney structures elsewhere in the Donghae-1 field. As reviewed in Beaudoin et al. (2014), a critical aspect of such production is the impact of transporting high-temperature fluid and gas up through overlying gas hydrate-bearing sediment.

Hadley et al. (2008) calculated that enough heat would be released into overlying, hydrate-bearing sediment from a conventional production well over its 30-year lifespan to dissociate gas hydrate 20–50 m away from the well. Their location, the Gumusut-Kakap field offshore Malaysia, was found via pressure coring to have primarily hydrate-filled veins in fine-grained sediment, similar to the hydrate morphology at UBGH2-3. When heated above its stability temperature, the gas hydrate will break down, releasing gas. Jang and Santamarina (2016b) show that at 10 MPa (~1000 m below sea level, which for UBGH2-3 would be

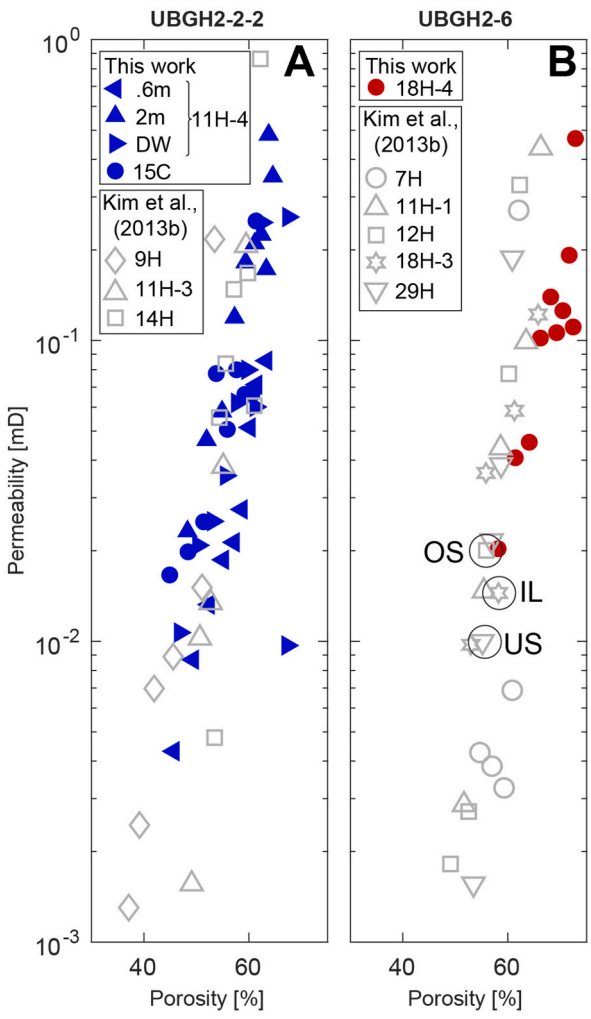

Fig. 13. Permeability dependence on porosity for (A) UBGH2-2-2B and (B) UBGH2-6. Solid symbols are results from this study and are available online (Jang et al., 2022a). Open symbols are from Kim et al. (2013b). All measurements are made during 1D consolidation tests using Terzaghi's et al. (1996) approach, so points for each sample plot at lower permeability and porosity values as the effective stress is increased. Peak stress is 2.56 MPa for this work, and 1.8 MPa for the Kim et al. (2013b) results. For UBGH2-6, the in situ effective stress at the gas hydrate reservoir is ~0.9 MPa (Kim et al., 2013b), a stress for which the measured permeabilities are on the order of 0.01mD. The three circled data points from Kim et al. (2013b) represent results indicative of the in situ permeabilities for the overlying sediment (OS), the fine-grained interbed layers (IL), and the underlying seal (US).

~100 mbsf), dissociation should cause a volume expansion of a factor of 2.4 as the hydrate reverts to water and gas at the stability temperature. This expansion factor increases as the in situ pressure decreases toward the seafloor and as the system warms further above the stability temperature due to heat from conventional hydrocarbons being pumped up from underlying sediment. Though diatoms increase the host sediment permeability relative to diatom-free sediment, the pore-throats in the fine-grained UBGH2-3 sediment are still too small to be conducive to gas entry, and the elevated gas pressure will fracture sediment around the hydrate-filled veins (Daigle et al., 2020; Jain and Juanes, 2009; Shin and Santamarina, 2011; Jang and Santamarina, 2016b).

Shiwakoti et al. (2002) note how cemented bonds can form between diatoms in situ. Such bonds will help the host sediment resist fracturing by increasing the tensile strength of the host sediment, but this is not likely to prevent sediment fracturing at an environment like UBGH2-3 because of the high overpressures that could develop. For example, Briaud and Chaouch (1997), in their modeling of hydrate dissociation around a conventional production well, note the production fluids are much warmer than the overlying hydrate-bearing sediment. They assume 100 °C fluids are pumped up the production well, but hydrate at the ~10 MPa pore pressure for UBGH2-3 will break down if the temperature exceeds 11.5 °C (using the hydrate/seawater stability curve from Tishchenko et al., 2005). Even just an additional 6 °C temperature increase can generate an 11 MPa pressure increase (Tishchenko et al., 2005). Shiwakoti et al. (2002) present SEM imagery indicating extensive diatom crushing occurs when diatoms are subjected to 10 MPa loads, and as noted above, Shiwakoti et al. (2002) measure a dramatic increase in sediment compressibility when diatom-rich sediment is subjected to even 200 kPa loads. The significant pressure increase that can occur during hydrate dissociation via warming for a site such as UBGH2-3 can be expected to fracture the host sediment even in the presence of high diatom concentrations (22–34% by volume at UBGH2-3, Table 7).

Hadley et al. (2008) consider the potential for these depressurization-induced fractures to reach the seafloor to allow direct methane escape to the water column. The gas-generated fractures can buckle the well itself, via stress transfer to the well or by causing sediment subsidence around the well (Hadley et al., 2008). Gas can also migrate to the well and then up the well casing to the surface (Collett and Dallimore, 2002; Beaudoin et al., 2014). In total, the hydrate-related risks to conventional hydrocarbon production at the Gumusut-Kakap field were considered high enough that the well site location and clustered well approach were both changed to reduce exposure to the hydrate-bearing sediment (Hadley et al., 2008). For UBGH2-3, the presence of diatoms does not appear to provide a sufficient sediment strength increase to merit locating a conventional hydrocarbon well in the chimney feature's vicinity.

7. Conclusions

Whether gas hydrate or underlying conventional hydrocarbons can be economically recovered as an energy resource depends, in part, on the properties of sediment associated with the gas hydrate. A common feature of the recovered sediment associated with gas hydrate from the four UBGH2 sites tested here is the presence of diatoms, which exist in large enough concentrations to alter the overall sediment properties.

Diatoms are typically considered to increase both sediment compressibility and permeability, but in our study, the diatom influence was easier to observe in sediment compressibility than in permeability. Whereas the compressibility scaled with increasing diatom content, a permeability shift to higher values was only apparent for the highest diatom content (~45%). Even accounting for the high diatom-content specimen, the in situ permeability for these fine-grained sediments is likely to be on the order of 0.01mD, which is slightly lower than the 0.02 mD permeability measured for diatom-free sediment of a very similar grain size from offshore India (Jang et al., 2019a).

Implications for extracting methane from gas hydrate hosted in thinly-layered, coarse-grained sediment interbedded with, and bound by, the fine-grained sediment tested here (e.g., UBGH2-2-2B, UBGH2-6) are that any well design will need to account for interbeds and bounding seal sediment that is 70–170% more compressible than the reservoir sediment itself. If the well can sustain the sediment compaction as the reservoir pressure is drawn down, the interbeds and seal sediment should provide initially effective barriers to fluid flow because they are two orders of magnitude less permeable than the anticipated permeability of the hydrate-bearing sediment itself. Moreover, the permeability reduction due to compaction could reduce the interbed and seal permeability another order of magnitude.

The low density and high surface area of diatoms make them susceptible to resuspension. Lighter, more easily suspended sediment would benefit fluidization or other production techniques that bring all sediment, fluid and hydrate to the surface, but when utilizing depressurization in conventional wells, preferential fluid and gas flow along

the interfaces between the reservoir and interbed or seal sediment is likely to draw diatom-rich fines toward the well where they could clog pore throats and reduce production efficiency.

When attempting to draw relatively warm conventional hydrocarbons up through a well that penetrates hydrate-bearing sediment in these deep-water systems (e.g., UBGH2-3), the potential bonding between diatoms will not likely provide enough sediment strength increase to withstand the pore pressure increase as gas hydrate dissociates via heating around the conventional well. The low measured permeability, even in the presence of diatoms, will exacerbate any pressure increase during dissociation by limiting the extent to which fluid can flow away from the dissociation fronts.

Overall, diatoms in undisturbed sediment have the capacity to increase sediment strength due to diatom-diatom bonding, and the presence of diatoms can increase permeability and porosity, but at the water depths characteristic of these UBGH2 sites, methane or hydrocarbon extraction is anticipated to impose effective stress increases of 3–15 MPa that will significantly disturb the diatom-rich sediment. Our measurements suggest we can anticipate that the mechanical behavior of the fine-grained UBGH2 sediment at the four sites in this study will be dominated by the diatom behavior in disturbed sediment. We anticipate the sediment to be compressible and low-permeability, and that these properties will not be significantly influenced by any pore-water freshening that occurs as a result of hydrate dissociation.

Declaration of competing interest

The authors declare that they have no known competing financial interests or personal relationships that could have appeared to influence the work reported in this paper.

Data availability

As noted in the text, experimental data are available online from Jang et al. (2022a and b in the reference list).

Acknowledgements

This work was supported by the National Research Foundation of Korea (NRF) grant funded by the Korea government (MSIT, Ministry of Science and ICT) (No. NRF-2021R1F1A1060406) and by KIGAM's "Gas Hydrate Exploration and Production Study" project (Grant No. GP2016-027/GP2021-011), managed and funded by GHDO (Gas Hydrate R&D Organization) and MOTIE (Ministry of Trade, Industry and Energy) and also supported by the Basic Research Project (GP2020-025) of KIGAM, funded by MSIT. This work was also supported by the U.S. Department of Energy (DOE) through interagency agreements (DE-FE0023495, DE-FE00-26166 and 89243320SFE000013) with the U.S. Geological Survey (USGS) and by the USGS Coastal and Marine Hazards and Resources Program. As noted in the text, experimental data are available online (see Jang et al., 2022a, 2022b in the reference list). Any use of trade, firm, or product names is for descriptive purposes only and does not imply endorsement by the U.S. Government.

References

Ajayi, T., Anderson, B.J., Seol, Y., Boswell, R., Myshakin, E.M., 2018. Key aspects of numerical analysis of gas hydrate reservoir performance: Alaska North Slope Prudhoe Bay Unit "L-Pad" hydrate accumulation. J. Nat. Gas Sci. Eng. 51, 37–43. https://doi.org/10.1016/j.jngse.2017.12.026.

Anderson, B., Boswell, R., Collett, T.S., Farrell, H., Ohtsuki, S., White, M., Zyrianova, M., 2014. Review of the findings of the Ignik Sikumi CO2-CH4 gas hydrate exchange field trial. In: Proceedings of the 8th International Conference on Gas Hydrates. United States: China Geological Survey, Beijing, China.

Anderson, A.L., Bryant, W.R., 1990. Gassy sediment occurrence and properties: northern Gulf of Mexico. Geo Mar. Lett. 10 (4), 209–220. https://doi.org/10.1007/BF02431067.

Archie, G.E., 1942. The electrical resistivity log as an aid in determining some reservoir characteristics. Trans. Am. Inst. Min. Metall. Petrol. Eng. 146, 54–62. https://doi.org/10.2118/942054-G.

ASTM, 2010. Standard Test Methods for Liquid Limit, Plastic Limit, and Plasticity Index of Soils, ASTM D4318. ASTM International, West Conshohocken, PA.

ASTM, 2011a. Standard Practice for Classification of Soils for Engineering Purposes (Unified Soil Classification System), ASTM D2487. ASTM, West Conshohocken, PA.

ASTM, 2011b. Standard Test Methods for One-Dimensional Consolidation Properties of Soils Using Incremental Loading, ASTM D2435. ASTM, West Conshohocken, PA.

Bahk, J.J., Kim, D.H., Chun, J.H., Son, B.K., Kim, J.H., Ryu, B.J., Torres, M.E., Riedel, M., Schultheiss, P., 2013a. Gas hydrate occurrences and their relation to host sediment properties: results from second Ulleung Basin gas hydrate drilling expedition, East Sea. Mar. Petrol. Geol. 47, 21–29. https://doi.org/10.1016/j.marpetgeo.2013.05.006.

Bahk, J.J., Kim, G.Y., Chun, J.H., Kim, J.H., Lee, J.Y., Ryu, B.J., Lee, J.H., Son, B.K., Collett, T.S., 2013b. Characterization of gas hydrate reservoirs by integration of core and log data in the Ulleung Basin, East Sea. Mar. Petrol. Geol. 47, 30–42. https://doi.org/10.1016/j.marpetgeo.2013.05.007.

Beaudoin, Y.C., Dallimore, S.R., Boswell, R., 2014. Frozen Heat: A UNEP Global Outlook on Methane Gas Hydrates, vol. 2. United Nations Environment Programme, GRID-Arendal.

Bolt, G.H., 1956. Physico-chemical analysis of the compressibility of pure clays. Geotechnique 6 (2), 86–93. https://doi.org/10.1680/geot.1956.6.2.86.

Boswell, R., Collett, T.S., 2011. Current perspectives on gas hydrate resources. Energy Environ. Sci. 4 (4), 1206–1215. https://doi.org/10.1039/c0ee00203h.

Boswell, R., Myshakin, E., Moridis, G., Konno, Y., Collett, T.S., Reagan, M., Ajayi, T., Seol, Y., 2019. India National Gas Hydrate Program Expedition 02 summary of scientific results: numerical simulation of reservoir response to depressurization. Mar. Petrol. Geol. 108, 154–166. https://doi.org/10.1016/j.marpetgeo.2018.09.026.

Boswell, R., Yamamoto, K., Lee, S.R., Collett, T., Kumar, P., Dallimore, S., 2014. Chapter 8 - methane hydrates. In: Letcher, T.M. (Ed.), Future Energy. Elsevier, Boston.

Briaud, J.L., Chaouch, A., 1997. Hydrate melting in soil around hot conductor. J. Geotech. Geoenviron. Eng. 123 (7), 645–653. https://doi.org/10.1061/(ASCE)1090-0241(1997)123:7(645).

British Standard Institute, B.S.I., 1990. Methods of Test for Soils for Civil Engineering Purpose, BS 1377. BSI (British Standards Institution, London.

Cao, S.C., Jang, J., Jung, J., Waite, W.F., Collett, T.S., Kumar, P., 2019. 2D micromodel study of clogging behavior of fine-grained particles associated with gas hydrate production in NGHP-02 gas hydrate reservoir sediments. Mar. Petrol. Geol. 108, 714–730. https://doi.org/10.1016/j.marpetgeo.2018.09.010.

Cawthern, T., Johnson, J.E., Giosan, L., Flores, J.A., Rose, K., Solomon, E., 2014. A late miocene-early pliocene biogenic silica crash in the Andaman Sea and Bay of Bengal. Mar. Petrol. Geol. 58, 490–501. https://doi.org/10.1016/j.marpetgeo.2014.07.026.

Chough, S.K., Barg, E., 1987. Tectonic history of Ulleung Basin margin, East Sea (sea of Japan). Geology 15 (1), 45–48. https://doi.org/10.1130/0091-7613(1987)15<45:THOUBM>2.0.CO;2.

Collett, T.S., Dallimore, S.R., 2002. Detailed analysis of gas hydrate induced drilling and production Hazards. In: Proceedings Proceedings of the 4th International Conference on Gas Hydrates, pp. 47–52. Yokohama May 19-23.

Cortese, G., Gersonde, R., Hillenbrand, C.D., Kuhn, G., 2004. Opal sedimentation shifts in the world ocean over the last 15 Myr. Earth Planet Sci. Lett. 224 (3–4), 509–527. https://doi.org/10.1016/j.epsl.2004.05.035.

Dai, S., Boswell, R., Waite, W.F., Jang, J., Lee, J.Y., Seol, Y., June . What has been learned from pressure cores. In: Proceedings the 9th International Conference on Gas Hydrates. Denver, Colorado, USA.

Dai, S., Kim, J., Xu, Y., Waite, W.F., Jang, J., Collett, T.S., Kumar, P., 2019. Permeability anisotropy and relative permeability in sediments from the national gas hydrate Program expedition 02, offshore India. Mar. Petrol. Geol. 108, 705–713. https://doi.org/10.1016/j.marpetgeo.2018.08.016.

Dai, S., Lee, J.Y., Santamarina, J.C., 2014. Hydrate nucleation in quiescent and dynamic conditions. Fluid Phase Equil. 378, 107–112. https://doi.org/10.1016/j.fluid.2014.07.006.

Daigle, H., Cook, A., Fang, Y., Bihani, A., Song, W., Flemings, P.B., 2020. Gas-driven tensile fracturing in shallow marine sediments. J. Geophys. Res. Solid Earth 125 (12), e2020JB020835. https://doi.org/10.1029/2020JB020835.

Daigle, H., Dugan, B., 2010. Origin and evolution of fracture-hosted methane hydrate deposits. J. Geophys. Res. Solid Earth 115, B11103. https://doi.org/10.1029/2010jb007492.

Day, R.W., 1995. Engineering properties of diatomaceous fill. J. Geotech. Eng. 121 (12), 908–910. https://doi.org/10.1061/(ASCE)0733-9410(1995)121:12(908).

Dornan, P., Alavi, S., Woo, T.K., 2007. Free energies of carbon dioxide sequestration and methane recovery in clathrate hydrates. J. Chem. Phys. 127 (12) https://doi.org/10.1063/1.2769634. Artn 124510.

Falkner, R., 2016. The Paris Agreement and the new logic of international climate politics. Int. Aff. 95 (5), 1107–1125. https://doi.org/10.1111/1468-2346.12708.

Flemings, P.B., Phillips, S.C., Boswell, R., Collett, T.S., Cook, A.E., Dong, T.N., Frye, M., Goldberg, D.S., Guerin, G., Holland, M.E., Jang, J.B., Meazell, K., Morrison, J., O'Connell, J.I., Petrou, E.G., Pettigrew, T., Polito, P.J., Portnov, A., Santra, M., Schultheiss, P.J., Seol, Y., Shedd, W., Solomon, E.A., Thomas, C.M., Waite, W.F., You, K.H., 2020. Pressure coring a Gulf of Mexico deep-water turbidite gas hydrate reservoir: initial results from the University of Texas-Gulf of Mexico 2-1 (UT-GOM2-1) hydrate pressure coring expedition. AAPG Bull. 104 (9), 1847–1876. https://doi.org/10.1306/05212019052.

Hadley, C., Peters, D., Vaughan, A., Bean, D., 2008. Gumusut-Kakap project: geohazard characterisation and impact on field development plans (IPTC 12554). In:

International Petroleum Technology Conference. Kuala Lumpur, Malaysia. https://doi.org/10.2523/IPTC-12554-MS.
Halkos, G.E., Gkampoura, E.C., 2020. Reviewing usage, potentials, and limitations of renewable energy sources. Energies 13 (11). https://doi.org/10.3390/en13112906. ARTN. 2906.
Hancock, S., Boswell, R., Collett, T., 2019. Development of Deepwater Natural Gas Hydrates. Offshore Technology Conference, Houston, Texas. https://doi.org/10.4043/29374-MS. May 6-9. OTC-29374-MS.
Helgerud, M.B., Dvorkin, J., Nur, A., Sakai, A., Collett, T., 1999. Elastic-wave velocity in marine sediments with gas hydrates: effective medium modeling. Geophys. Res. Lett. 26 (13), 2021–2024. https://doi.org/10.1029/1999gl900421.
Hyndman, R.D., Davis, E.E., 1992. A mechanism for the formation of methane hydrate and sea-floor bottom-simulating reflectors by vertical fluid expulsion. J. Geophys. Res. Solid Earth 97 (B5), 7025–7041. https://doi.org/10.1029/91jb03061.
Ingle, J.C., 1992. Subsidence of the Japan Sea: stratigraphic evidence from ODP sites and onshore sections. In: Tamaki, K., Suyehiro, K., Allan, J., McWilliams, M. (Eds.), Proc. Ocean Drill. Progr. Sci. Results 127/128, 1197–1218. https://doi.org/10.2973/odp.proc.sr.127128-2.132.1992 part 2: College Station, TX.
Jain, A.K., Juanes, R., 2009. Preferential Mode of gas invasion in sediments: grain-scale mechanistic model of coupled multiphase fluid flow and sediment mechanics. J. Geophys. Res. Solid Earth 114, B08101. https://doi.org/10.1029/2008jb006002.
Jang, J., Santamarina, J.C., 2016a. Fines classification based on sensitivity to pore-fluid chemistry. J. Geotech. Geoenviron. Eng. 142 (4), 06015018. Artn 0601501810.1061/(Asce)Gt.1943-5606.0001420.
Jang, J., Santamarina, J.C., 2016b. Hydrate bearing clayey sediments: formation and gas production concepts. Mar. Petrol. Geol. 77, 235–246. https://doi.org/10.1016/j.marpetgeo.2016.06.013.
Jang, J., Cao, S.C., Stern, L.A., Jung, J., Waite, W.F., 2018. Impact of pore fluid chemistry on fine-grained sediment fabric and compressibility. J. Geophys. Res. Solid Earth 123 (7), 5495–5514. https://doi.org/10.1029/2018jb015872.
Jang, J., Dai, S., Yoneda, J., Waite, W.F., Stern, L., Boze, L., Collett, T.S., Kumar, P., 2019a. Pressure core analysis on geomechanical and fluid flow properties of a seal layer from the Krishna-Godavari Basin, offshore India. Mar. Petrol. Geol. 108, 537–550. https://doi.org/10.1016/j.marpetgeo.2018.08.015.
Jang, J., Waite, W.F., Stern, L., Collett, T.S., Kumar, P., 2019b. Physical property characteristics of gas hydrate-bearing reservoir and associated seal sediments collected during NGHP-02 in the Krishna-Godavari Basin, in the offshore of India. Mar. Petrol. Geol. 108, 249–271. https://doi.org/10.1016/j.marpetgeo.2018.09.027.
Jang, J., Cao, S.C., Stern, L.A., Waite, W.F., Jung, J., Lee, J.Y., 2020a. Potential freshening impacts on fines migration and pore-throat clogging during gas hydrate production: 2-D micromodel study with Diatomaceous UBGH2 sediments. Mar. Petrol. Geol. 116 https://doi.org/10.1016/j.marpetgeo.2020.104244. ARTN. 104244.
Jang, J., Waite, W.F., Stern, L.A., 2020b. Gas hydrate petroleum systems: what constitutes the "seal"? Interpretation-a J. Subsurf. Char. 8 (2), T231–T248. https://doi.org/10.1190/Int-2019-0026.1.
Jang, J., Waite, W.F., Stern, L.A., Lee, J.Y., 2022a. Dataset of diatom controls on the compressibility and permeability of fine-grained sediment collected offshore of South Korea during the Second Ulleung Basin Gas Hydrate Expedition, UBGH2. U.S. Geological Survey data release. https://doi.org/10.5066/P9ZLO4IM.
Jang, J., Waite, W.F., Stern, L.A., Lee, J.Y., 2022b. Dataset of diatom controls on the sedimentation behavior of fine-grained sediment collected offshore of South Korea during the Second Ulleung Basin Gas Hydrate Expedition, UBGH2. U.S. Geological Survey data release. https://doi.org/10.5066/P9S6S24N.
Jung, J.W., Jang, J., Santamarina, J.C., Tsouris, C., Phelps, T.J., Rawn, C.J., 2012. Gas production from hydrate-bearing sediments: the role of fine particles. Energy Fuels 26 (1), 480–487. https://doi.org/10.1021/ef101651b.
Kamatani, A., Riley, J.P., 1979. Rate of dissolution of diatom silica walls in seawater. Mar. Biol. 55, 29–35.
Kastner, M., Myers, M., Koh, C.A., Moridis, G.M., Johnson, J.E., Thurmond, J., 2022. Energy transition and climate mitigation require increased effort on methane hydrate Research. Energy Fuels 36 (6). https://doi.org/10.1021/acs.energyfuels.2c00338.
Kim, A.R., Kim, H.S., Cho, G.C., Lee, J.Y., 2017. Estimation of model parameters and properties for numerical simulation on geomechanical stability of gas hydrate production in the Ulleung Basin, East Sea, Korea. Quat. Int. 459, 55–68. https://doi.org/10.1016/j.quaint.2017.09.028.
Kim, G.Y., Narantsetseg, B., Ryu, B.J., Yoo, D.G., Lee, J.Y., Kim, H.S., Riedel, M., 2013a. Fracture orientation and induced anisotropy of gas hydrate-bearing sediments in seismic chimney-like-structures of the Ulleung Basin, East Sea. Mar. Petrol. Geol. 47, 182–194. https://doi.org/10.1016/j.marpetgeo.2013.06.001.
Kim, G.Y., Yi, B.Y., Yoo, D.G., Ryu, B.J., Riedel, M., 2011. Evidence of gas hydrate from downhole logging data in the Ulleung Basin, East Sea. Mar. Petrol. Geol. 28, 1979–1985. https://doi.org/10.1016/j.marpetgeo.2011.01.011.
Kim, H.S., Cho, G.C., Lee, J.Y., Kim, S.J., 2013b. Geotechnical and geophysical properties of deep marine fine-grained sediments recovered during the second Ulleung Basin Gas Hydrate expedition, East Sea, Korea. Mar. Petrol. Geol. 47, 56–65. https://doi.org/10.1016/j.marpetgeo.2013.05.009.
Kim, H.S., Riedel, M., Ryu, B.J., Kim, G.Y., Bahk, J.J., 2013c. Improving gas hydrate saturation estimates using P-wave velocity log data by incorporating XRD-data for detailed matrix-mineralogy definition. Mar. Petrol. Geol. 47, 155–167. https://doi.org/10.1016/j.marpetgeo.2013.05.020.
Kim, J.-H., Torres, M.E., Hong, W.-L., Choi, J., Michael, R., Bahk, J.-J., Kim, S.-H., 2013d. Pore fluid chemistry from the second gas hydrate drilling expedition in the Ulleung Basin (UBGH2): source, mechanisms and consequences of fluid freshening in the central part of the Ulleung Basin, East Sea. Mar. Petrol. Geol. 47, 99–112. https://doi.org/10.1016/j.marpetgeo.2012.12.011.
Konno, Y., Kato, A., Yoneda, J., Oshima, M., Kida, M., Jin, Y., Nagao, J., Tenma, N., 2019. Numerical analysis of gas production potential from a gas-hydrate reservoir at Site NGHP-02-16, the Krishna-Godavari basin offshore India - feasibility of depressurization method for ultra-deepwater environment. Mar. Petrol. Geol. 108, 731–740. https://doi.org/10.1016/j.marpetgeo.2018.08.001.
Kraemer, L.M, Owen, R.M., Dickens, G.R., 2000. Lithology of the upper gas hydrate zone, Blake Outer Ridge: a link between diatoms, porosity, and gas hydrate. In: Paull, C.K., Matsumoto, R., Wallace, P.J, Dillon, W.P. (Eds.), *Proceedings of the Ocean Drilling Program: Leg 164 Scientific Results*. Ocean Drilling Program, pp. 229–236. https://doi.org/10.2973/odp.proc.sr.164.221.2000.
Kvenvolden, K.A., 1993. Gas hydrates - geological perspective and global change. Rev. Geophys. 31 (2), 173–187. https://doi.org/10.1029/93rg00268.
Kvenvolden, K.A., Ginsburd, G.D., Soloviev, V.A., 1993. Worldwide distribution of subaquatic gas hydrates. Geo Mar. Lett. 13, 32–40. https://doi.org/10.1007/BF01204390.
Kwon, T.H., Lee, K.R., Cho, G.C., Lee, J.Y., 2011. Geotechnical properties of deep oceanic sediments recovered from the hydrate occurrence regions in the Ulleung Basin, East Sea, offshore Korea. Mar. Petrol. Geol. 28 (10), 1870–1883. https://doi.org/10.1016/j.marpetgeo.2011.02.003.
Lambe, T.W., Whitman, R.V., 1969. Soil Mechanics. John Wiley & Sons, New York.
Lee, C., Yun, T.S., Lee, J.S., Bahk, J.J., Santamarina, J.C., 2011. Geotechnical characterization of marine sediments in the Ulleung Basin, East Sea. Eng. Geol. 117, 151–158. https://doi.org/10.1016/j.enggeo.2010.10.014.
Lee, G.H., Kim, H.J., Han, S.J., Kim, D.C., 2001. Seismic stratigraphy of the deep Ulleung Basin in the East sea (Japan sea) back-arc basin. Mar. Petrol. Geol. 18 (5), 615–634. https://doi.org/10.1016/S0264-8172(01)00016-2.
Lee, J.S., Lee, J.Y., Kim, Y.M., Lee, C., 2013a. Stress-dependent and strength properties of gas hydrate-bearing marine sediments from the Ulleung Basin, East Sea, Korea. Mar. Petrol. Geol. 47, 66–76. https://doi.org/10.1016/j.marpetgeo.2013.04.006.
Lee, J.Y., Jung, J.W., Lee, M.H., Bahk, J.J., Choi, J., Ryu, B.J., Schultheiss, P., 2013b. Pressure core based study of gas hydrates in the Ulleung Basin and implication for geomechanical controls on gas hydrate occurrence. Mar. Petrol. Geol. 47, 85–98. https://doi.org/10.1016/j.marpetgeo.2013.05.021.
Lee, M.W., Collett, T.S., 2013. Scale-dependent gas hydrate saturation estimates in sand reservoirs in the Ulleung Basin, East Sea of Korea. Mar. Petrol. Geol. 47, 168–181. https://doi.org/10.1016/j.marpetgeo.2012.09.003.
Lei, L., Santamarina, J.C., 2018. Laboratory strategies for hydrate formation in fine-grained sediments. J. Geophys. Res. Solid Earth 123 (4), 2583–2596. https://doi.org/10.1002/2017jb014624.
Levi, M., 2013. Climate consequences of natural gas as a bridge fuel. Climatic Change 118 (3–4), 609–623. https://doi.org/10.1007/s10584-012-0658-3.
Li, B., Xu, T.F., Zhang, G.B., Guo, W., Liu, H.N., Wang, Q.W., Qu, L.L., Sun, Y.H., 2018. An experimental study on gas production from fracture-filled hydrate by CO2 and CO2/N-2 replacement. Energy Convers. Manag. 165, 738–747. https://doi.org/10.1016/j.enconman.2018.03.095.
Liu, L.P., Sun, Z.L., Zhang, L., Wu, N.Y., Qin, Y.C., Jiang, Z.Z., Geng, W., Cao, H., Zhang, X.L., Zhai, B., Xu, C.L., Shen, Z.C., Jia, Y.G., 2019. Progress in global gas hydrate development and production as a new energy resource. Acta Geol. Sin.-English Ed. 93 (3), 731–755. https://doi.org/10.1111/1755-6724.13876.
Mao, P.X., Wan, Y.Z., Sun, J.X., Li, Y.L., Hu, G.W., Ning, F.L., Wu, N.Y., 2021. Numerical study of gas production from fine-grained hydrate reservoirs using a multilateral horizontal well system. Appl. Energy 301. https://doi.org/10.1016/j.apenergy.2021.117450. ARTN. 117450.
Matsumoto, R., Tanahashi, M., Kakuwa, Y., Snyder, G., Ohikawa, S., Tomaru, H., Morita, S., 2017. Recovery of thick deposits of massive hydrates from gas chimney structures, eastern margin of Japan Sea: Japan Sea Shallow Gas Hydrate Project. Fire Ice: Dep. Energy, Off. Fossil Energy, Natl. Energy Technol. Lab. 17 (2), 1–6.
Mohan, K.K., Vaidya, R.N., Reed, M.G., Fogler, H.S., 1993. Water sensitivity of sandstones containing swelling and non-swelling clays. Colloids Surf. A Physicochem. Eng. Asp. 73, 237–254. https://doi.org/10.1016/0927-7757(93)80019-B.
Moridis, G.J., Reagan, M.T., Queiruga, A.F., Boswell, R., 2019a. Evaluation of the performance of the oceanic hydrate accumulation at site NGHP-02-09 in the Krishna-Godavari Basin during a production test and during single and multi-well production scenarios. Mar. Petrol. Geol. 108, 660–696. https://doi.org/10.1016/j.marpetgeo.2018.12.001.
Moridis, G.J., Reagan, M.T., Queiruga, A.F., Kim, S.J., 2019b. System response to gas production from a heterogeneous hydrate accumulation at the UBGH2-6 site of the Ulleung basin in the Korean East Sea. J. Petrol. Sci. Eng. 178, 655–665. https://doi.org/10.1016/j.petrol.2019.03.058.
Moridis, G.J., Sloan, E.D., 2007. Gas production potential of disperse low-saturation hydrate accumulations in oceanic sediments. Energy Convers. Manag. 48, 1834–1849. https://doi.org/10.1016/j.enconman.2007.01.023.
Myshakin, E., Lin, J.S., Uchida, S., Seol, Y., Collett, T., Boswell, R., 2019. Numerical simulation of depressurization-induced gas production from an interbedded turbidite hydrate-bearing sedimentary section in the offshore of India: site NGHP-02-16 (Area-B). Mar. Petrol. Geol. 108, 619–638. https://doi.org/10.1016/j.marpetgeo.2018.10.047.
Nagaraj, T.S., Murthy, B.R.S., 1986. A critical reappraisal of compression index equations. Geotechnique 36 (1), 27–32. https://doi.org/10.1680/geot.1986.36.1.27.
Ning, F., Chen, Q., Sun, J., Wu, X., Cui, G., Mao, P., Li, Y., Liu, T., Jiang, G., Wu, N., 2022. Enhanced gas production of silty clay hydrate reservoirs using multilateral wells and reservoir reformation techniques: numerical simulations. Energy 254, 124220. https://doi.org/10.1016/j.energy.2022.124220.

Olson, R.E., Mesri, G., 1970. Mechanisms controlling compressibility of clays. J. Soil Mech. Found. Div. Proc. Am. Soc. Civ. Eng. 96 (SM6), 1863–1878. https://doi.org/10.1061/JSFEAQ.0001475.

Oti, E.A., Cook, A.E., Welch, S.A., Sheets, J.M., Crandall, D., Rose, K., Daigle, H., 2019. Hydrate-filled fracture formation at Keathley Canyon 151, Gulf of Mexico, and implications for non-vent sites. Geochem. Geophys. Geosyst. 20 (11), 4723–4736. https://doi.org/10.1029/2019gc008637.

Oyama, H., Abe, S., Yoshida, T., Sato, T., Nagao, J., Tenma, N., Narita, H., 2016. Experimental study of mud erosion at the interface of an artificial sand-mud alternate layer. J. Nat. Gas Sci. Eng. 34, 1106–1114. https://doi.org/10.1016/j.jngse.2016.07.067.

Park, Y., Kim, D.Y., Lee, J.W., Huh, D.G., Park, K.P., Lee, J., Lee, H., 2006. Sequestering carbon dioxide into complex structures of naturally occurring gas hydrates. Proc. Natl. Acad. Sci. U. S. A. 103 (34), 12690–12694. https://doi.org/10.1073/pnas.0602251103.

Priest, J.A., Hayley, J.L., Smith, W.E., Schultheiss, P., Roberts, J., 2019. PCATS triaxial testing: geomechanical properties of sediments from pressure cores recovered from the Bay of Bengal during Expedition NGHP-02. Mar. Petrol. Geol. 108, 424–438. https://doi.org/10.1016/j.marpetgeo.2018.07.005.

Riedel, M., Bahk, J.J., Scholz, N.A., Ryu, B.J., Yoo, D.G., Kim, W., Kim, G.Y., 2012. Mass-transport deposits and gas hydrate occurrences in the Ulleung Basin, East Sea - Part 2: gas hydrate content and fracture-induced anisotropy. Mar. Petrol. Geol. 35 (1), 75–90. https://doi.org/10.1016/j.marpetgeo.2012.03.005.

Ryu, B.J., Collett, T.S., Riedel, M., Kim, G.Y., Chun, J.H., Bahk, J.J., Lee, J.Y., Kim, J.H., Yoo, D.G., 2013. Scientific results of the second gas hydrate drilling expedition in the Ulleung Basin (UBGH2). Mar. Petrol. Geol. 47, 1–20. https://doi.org/10.1016/j.marpetgeo.2013.07.007.

Ryu, B.J., Riedel, M., Kim, J.H., Hyndman, R.D., Lee, Y.J., Chung, B.H., Kim, I.S., 2009. Gas hydrates in the western deep-water Ulleung Basin, East Sea of Korea. Mar. Petrol. Geol. 26 (8), 1483–1498. https://doi.org/10.1016/j.marpetgeo.2009.02.004.

Santamarina, J.C., Dai, S., Jang, J., Terzariol, M., 2012. Pressure core characterization tools for hydrate-bearing sediments. Sci. Drill. J. 14, 44–48. https://doi.org/10.2204/iodp.sd.14.06.2012.

Santamarina, J.C., Klein, K.A., Wang, Y.H., Prencke, E., 2002. Specific surface: determination and relevance. Can. Geotech. J. 39 (1), 233–241. https://doi.org/10.1139/T01-077.

Schicks, J.M., Luzi, M., Beeskow-Strauch, B., 2011. The conversion process of hydrocarbon hydrates into CO2 hydrates and vice versa: thermodynamic considerations. J. Phys. Chem. A 115 (46), 13324–13331. https://doi.org/10.1021/jp109812v.

Schicks, J.M., Strauch, B., Heeschen, K.U., Spangenberg, E., Luzi-Helbing, M., 2018. From microscale (400μl) to macroscale (425L): experimental investigations of the CO2/N-2-CH4 exchange in gas hydrates simulating the Ignik Sikumi field trial. J. Geophys. Res. Solid Earth 123 (5), 3608–3620. https://doi.org/10.1029/2017jb015315.

Schoderbeck, D., Farrell, H., Hester, K., Howard, J., Raterman, K., Silpngarmlert, K.L., Martin, K.L., Smith, B., Klein, P., 2013. ConocoPhillips Gas Hydrate Production Test Final Technical Report. National Energy Technology Laboratory.

Schultheiss, P.J., Holland, M., Humphrey, G., 2009. Wireline coring and analysis under pressure: recent use and future developments of the HYACINTH system. Sci. Drill. J. 7, 44–50. https://doi.org/10.2204/iodp.sd.7.07.2009.

Shin, H., Santamarina, J.C., 2011. Open-mode discontinuities in soils. Géotech. Lett. 1, 95–99. https://doi.org/10.1680/geolett.11.00014.

Shiwakoti, D.R., Tanaka, H., Tanaka, M., Locat, J., 2002. Influences of diatom microfossils on engineering properties of soils. Soils Found. 42 (3), 1–17. https://doi.org/10.3208/sandf.42.3_1.

Skempton, A.W., Jones, O.T., 1944. Notes on the compressibility of clays. Q. J. Geol. Soc. 100 (1–4), 119–135. https://doi.org/10.1144/GSL.JGS.1944.100.01-04.08.

Sloan, E.D., Koh, C.A., 2007. Clathrate Hydrates of Natural Gases. CRC Press, Taylor & Francis Group, LLC, New York.

Tanaka, K., Cavalett, O., Collins, W.J., Cherubini, F., 2019. Asserting the climate benefits of the coal-to-gas shift across temporal and spatial scales. Nat. Clim. Change 9 (5), 389–396. https://doi.org/10.1038/s41558-019-0457-1.

Taylor, D.W., 1948. Fundamentals of Soil Mechanics. John Wiley&Sons, Inc., New York.

Terzaghi, K., Peck, R.B., Mesri, G., 1996. Soil Mechanics in Engineering Practice. John Wiley & Sons, Inc., New York.

Thomas, C., Phillips, S.C., Flemings, P.B., Santra, M., Hammon, H., Collett, T.S., Cook, A. E., Pettigrew, T., Mimitz, M., Holland, M., Schultheiss, P., 2020. Pressure coring operations during the University of Texas-Gulf of Mexico 2-1 (UT-GOM2-1) hydrate pressure coring expedition in green Canyon block 955, northern Gulf of Mexico. AAPG Bull. 104 (9), 1877–1901. https://doi.org/10.1306/02262019036.

Tishchenko, P., Hensen, C., Wallmann, K., Wong, C.S., 2005. Calculation of the stability and solubility of methane hydrate in seawater. Chem. Geol. 219, 37–52. https://doi.org/10.1016/j.chemgeo.2005.02.008.

Treguer, P., Nelson, D.M., Van Bennekom, A.J., DeMaster, D.J., Leynaert, A., Queguiner, B., 1995. The silica balance in the world ocean: a reestimate. Science 268 (5209), 375–379. https://doi.org/10.1126/science.268.5209.375.

Uchida, S., Lin, J.S., Seol, Y., Collett, T., Boswell, R., 2019. Numerical simulation of sand production in interbedded hydrate-bearing sediments at Site NGHP-02-16. Mar. Petrol. Geol. 108, 639–647. https://doi.org/10.1016/j.marpetgeo.2018.10.046.

U.N. Framework Convention on Climate Change, 2016. Report of the conference of the parties on its twenty-first session. In: Held in Paris from 30 November to 13 December 2015, Part Two: Action Taken by the Conference of the Parties at its Twenty-First Session. https://unfccc.int/sites/default/files/resource/docs/2015/cop21/eng/10a01.pdf.

Valdes, J.R., Santamarina, J.C., 2007. Particle transport in a nonuniform flow field: retardation and clogging. Appl. Phys. Lett. 90 (24), 244101 https://doi.org/10.1063/1.2748850.

Waite, W.F., Ruppel, C.D., Boze, L.G., Lorenson, T.D., Buckzowski, B.J., McMullen, K., Kvenvolden, K.A., 2020. Preliminary global database of known and inferred gas hydrate locations. U.S. Geol. Surv. Data Release. https://doi.org/10.5066/P9llFVJM.

Wallmann, K., Pinero, E., Burwicz, E., Haeckel, M., Hensen, C., Dale, A., Ruepke, L., 2012. The global inventory of methane hydrate in marine sediments: a theoretical approach. Energies 5 (7), 2449–2498. https://doi.org/10.3390/en5072449.

Wentworth, C.K., 1922. A scale of grade and class terms for clastic sediments. Geology 30 (5), 377–392. https://www.jstor.org/stable/30063207.

Wroth, C.P., Wood, D.M., 1978. The correlation of index properties with some basic engineering properties of soils. Can. Geotech. J. 15 (2), 137–145. https://doi.org/10.1139/t78-014.

Yamamoto, K., Kanno, T., Wang, X.X., Tamaki, M., Fujii, T., Chee, S.S., Wang, X.W., Pimenov, V., Shako, V., 2017. Thermal responses of a gas hydrate-bearing sediment to a depressurization operation. RSC Adv. 7 (10), 5554–5577. https://doi.org/10.1039/c6ra26487e.

Yamamoto, K., Suzuki, K., Wang, X., Matsunaga, T., Nishioka, I., Nakatsuka, Y., Yoneda, J., 2019. The second offshore production test of methane hydrates in the Eastern Nankai Trough and site characterization efforts. Fire Ice: Dep. Energy, Off. Fossil Energy, Natl. Energy Technol. Lab. 19 (1), 9–15.

Ye, J., Wei, J., Liang, J., Lu, J., Lu, H., Zhang, W., 2019. Complex gas hydrate system in a gas chimney, South China Sea. Mar. Petrol. Geol. 104, 29–39. https://doi.org/10.1016/j.marpetgeo.2019.03.023.

Yoneda, J., Kida, M., Konno, Y., Jin, Y., Morita, S., Tenma, N., 2019a. In situ mechanical properties of shallow gas hydrate deposits in the deep seabed. Geophys. Res. Lett. 46 (24), 14459–14468. https://doi.org/10.1029/2019gl084668.

Yoneda, J., Oshima, M., Kida, M., Kato, A., Konno, Y., Jin, Y., Jang, J., Waite, W.F., Kumar, P., Tenma, N., 2019b. Permeability variation and anisotropy of gas hydrate-bearing pressure-core sediments recovered from the Krishna–Godavari Basin, offshore India. Mar. Petrol. Geol. 108, 524–536. https://doi.org/10.1016/j.marpetgeo.2018.07.006.

Yoo, D.G., Kang, N.K., Yi, B.Y., Kim, G.Y., Ryu, B.J., Lee, K., Lee, G.H., Riedel, M., 2013. Occurrence and seismic characteristics of gas hydrate in the Ulleung Basin, East Sea. Mar. Petrol. Geol. 47, 236–247. https://doi.org/10.1016/j.marpetgeo.2013.07.001.

Zglobicka, I., Li, Q., Gluch, J., Plocinska, M., Noga, T., Dobosz, R., Szoszkiewicz, R., Witkowski, A., Zschech, E., Kurzydlowski, K.J., 2017. Visualization of the internal structure of Didymosphenia geminata frustules using nano X-ray tomography. Sci. Rep. 7 https://doi.org/10.1038/s41598-017-08960-5. ARTN. 9086.

Zhang, W., Liang, J.Q., Wei, J.G., Lu, J.A., Su, P.B., Lin, L., Huang, W., Guo, Y.Q., Deng, W., Yang, X.L., Wan, Z.F., 2020. Geological and geophysical features of and controls on occurrence and accumulation of gas hydrates in the first offshore gas-hydrate production test region in the Shenhu area, Northern South China Sea. Mar. Petrol. Geol. 114 https://doi.org/10.1016/j.marpetgeo.2019.104191.